ACOUSTICS COMPARISON OF A NOVEL REDUCED TIP VORTEX ROTARY BLADE AND A TRADITIONAL BLADE

BY

MATEO DIAZ

THESIS

Submitted in partial fulfillment of the requirements
for the degree of Master of Science in Aerospace Engineering
in the Graduate College of the
University of Illinois Urbana-Champaign, 2021

Urbana, Illinois

Advisor:

Assistant Professor Theresa Saxton-Fox

ABSTRACT

Acoustics data collection was performed in an anechoic chamber for two propeller blade types, one traditional power optimized blade and one novel blade designed to reduce generated tip vortex strength. Both blade types had a 7.82” radius, a 2.25” root chord, a taper ratio of 2, a thrust coefficient of 0.003, and used an Eppler E387 airfoil. The blades were held at a steady 5000 rotations per minute as data were captured at 11 different microphone locations downwind of the rotor disc. Data were processed using a Fourier transform and analyzed. Key peaks in the processed data were identified and compared for each blade type and microphone location. Compared to the power optimized blade, the reduced vortex blade was found to have a greater number of distinct peaks. Additionally, for peaks that were present in the acoustic signatures of both blade types, the reduced vortex blade’s peaks were slightly greater in magnitude on average.

ACKNOWLEDGMENTS

I would like to start by extending my gratitude to my advisor, Professor Theresa Saxton-Fox. Her continued guidance and support over the past year has allowed me to achieve far more in my academic career than I ever could have alone. I would also like to extend this gratitude to my peers Aadhy Parthasarathy and Akhil Borra, who have also helped me immensely throughout the writing process, as well as Professor Phil Ansell, Daniel Yu, and CU Aerospace for their collaboration and assistance throughout the project.

Support of the Air Force through grant FA8649-21-P-0053 is gratefully acknowledged.

Third, I would like to thank Professor Jennifer Bernhard for allowing my colleagues and me to utilize the anechoic chamber at her laboratory. Her facility was just about the best place we could ask for to perform acoustic data collection.

Next, I would like to thank my late eldest brother who inspired me to pursue engineering when I was a teen. I wish you could be here with us today to see how far I have come.

Finally, I must give my most heartfelt thanks to my wonderful fiancée, Daniela, who has both inspired me with her own successes and encouraged me to reach for my own. I would not have been able to make it this far without her unwavering love and support.

TABLE OF CONTENTS

CHAPTER 1: INTRODUCTION

In this chapter, a variety of background information, such as the importance of rotorcraft acoustics and blade-vortex interaction (BVI), is detailed. Previous and potential future work are also discussed.

1.1 Rotorcraft Noise

Recent years have seen a significant increase in the use of rotorcraft, especially unmanned aerial vehicles (UAVs), for a variety of purposes. Many people use UAVs for recreation. Some simply fly them for fun, while others use them for hobbies like photography [1] and even competitive racing events [2]. In the commercial field, UAVs have been utilized in a wide range of applications. Real-estate agencies use UAVs to take pictures of houses [3], some companies fly them for security purposes [4], and Amazon is currently developing a system to deliver packages using UAVs called Amazon Air, which is already seeing use in limited circumstances [5]. Other rotorcraft, like helicopters, are commonly used by news stations and as emergency response vehicles. In the military field, rotorcraft have been used for several years already and new systems continue to be developed in a variety of usage applications, including surveillance, support, and supply delivery [6]. Speculations of future uses of rotorcraft are ambitious, with many of the aforementioned uses expected to increase in popularity with time and new ones appearing rapidly. Uber and Joby Aviation are developing an on-demand urban air transportation program, similar to an airborne version of Uber's current business model, called Uber Elevate which is intending to operate as soon as 2023 [7]. Such a program could see hordes of large rotorcraft being operated daily in many major cities, with especially high traffic during typical business commute hours.

With a rapidly growing fleet of rotorcraft being used worldwide, it is important to understand the acoustic characteristics of these vehicles.

These vehicles' ability to perform effectively in this wide range of roles is often due to the superior mobility and hovering capabilities that rotary wings provide, capabilities that have been unmatched by any other technology for decades. Being able to take off vertically and move freely in any direction allows for an aircraft to navigate difficult terrain easily, making it more suitable for a large range of environments. The ability to hover in place allows for rotorcraft to perform tasks that fixed wing vehicles cannot easily do, such as video surveillance. A significant drawback of rotary wings, however, is that they are often very noisy. For many recreationally and commercially used rotorcraft, the noise they produce can be a significant annoyance to the general public, especially for those vehicles operating in residential areas. A small commercial quadrotor UAV like the DJI Phantom 2, weighing just 1.6 kg, produces an effective perceived noise level (EPNL) of around 76 decibels (dB) at a distance of 5 meters during flyover [8], comparable to the volume of the average vacuum cleaner. The Federal Aviation Administration (FAA) does not currently have any noise regulations in place for aircraft this small, but significant increases in their use, such as for the aforementioned Amazon Air system, could possibly spark a need for them. Larger aircraft like those to be used for Uber Elevate are regulated by Title 14 of the Code of Federal Regulations (CFR) Part 36 [9]. The final specifications of the current proposed designs [10] are not available yet, but the Uber Elevate aircraft could be similar in size and form to the Joby S4, a small rotorcraft capable of carrying four passengers plus a pilot and having a gross weight of 2177 kg [11]. According to 14 CFR Part 36 Appendix K, such an aircraft would have a certification noise limit of about 94 dB EPNL for a 150 meter flyover. Uber has set their own, much more optimistic goal of 62 dB at 500 feet (152.4 m) [10]. For many military purposes, noise

produced by rotorcraft can significantly detract from their stealth. The rotor of a large tactical UAV under static conditions can produce peak blade pass sound pressure levels (SPL) between 80 and 105 dB at a distance of 25 meters, comparable to the volume of a motorcycle, before even factoring in engine noise [12]. If the usage of these rotorcraft is to be significantly expanded, the ability to identify and reduce significant contributors to the noise they produce will be extremely helpful.

There are a number of specific sources of noise produced by rotorcraft that can be targeted in order to reduce a vehicle's overall noise. First, engine and motor noise are significant contributors. For rotorcraft utilizing battery-powered electronic motors, this noise source is typically not very prominent, but for those powered by internal combustion engines, especially piston-engines, this noise can be one of the greatest [13]. The reduction of power required can mitigate noise production, as generally if a rotor does not have to work as hard to perform a certain task, it will not make as much noise. This reduction can be accomplished in a variety of ways, such as by improving the vehicle's aerodynamics or by reducing weight with lightweight components and materials. The way in which a rotorcraft operates can also affect the amount of noise produced. Maneuvers that involve sudden and rapid accelerations typically create more noise than slow and moderate ones, so the use of smoother flight paths can also help mitigate noise [14]. Weather conditions such as gusty winds can also cause a rotorcraft to produce more noise as frequent adjustments are required to maintain desired trajectories, though in many rotorcraft use cases little can be done to avoid such conditions outright. With the exception of engine and motor noise, the fluid dynamics of rotary wings is the basis of all the aforementioned sources of noise, so a good understanding of it is crucial to reducing the noise produced.

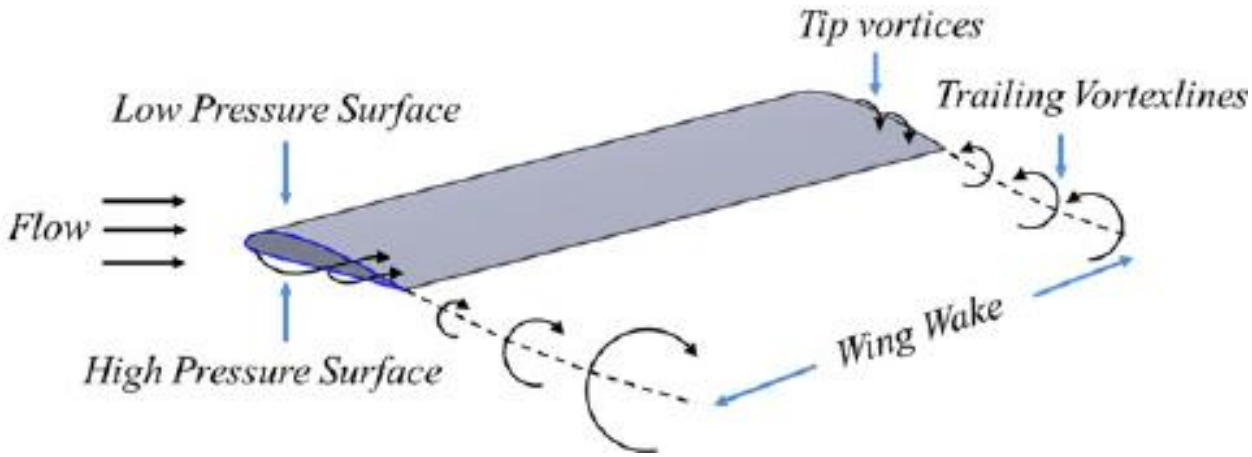

Figure 1.1: Wing tip vortex formation over a fixed wing [15]

1.2 Blade-Vortex Interaction

Any interaction between a fluid and a solid object can produce sound. How, then, can the noise production of an aircraft ever be eliminated? In all likelihood, it probably can never be completely eliminated, but it can be reduced. One factor of interest when it comes to noise reduction of rotorcraft is blade-vortex interaction (BVI). When a wing passes through a flow under typical flight conditions, regions of high-pressure air form beneath the wing and regions of low-pressure air form above it, as illustrated in Figure 1.1. As the flow continues, these regions undergo a continuous equalization of pressures, causing air to flow from the bottom of the wing to the top, moving around the wing tip. This results in the formation of a swirling vortex of air at each wing tip. The vortices then trail in a line behind the wing in the direction of the free stream, shown at the bottom and the right of Figure 1.1. For rotary wings, the process of vortex formation is largely the same. Each rotary wing equates to half of the fixed wing in the previous example, from its center to one of the wing tips, with one trail of vortices being created at each rotary wing tip. Additionally, because the speed of rotation of the blades is typically much greater than the free stream velocity, the vortices leave trails in a cycloid-like shape rather than a line, as illustrated in Figure 1.2. Due to this shape of the trailed vortices, often when a vortex forms from one blade, the

next blade that passes through its space collides with the vortex, causing a BVI. If other rotors are also present, such as the helicopter tail rotor shown at the bottom right of Figure 1.2, then BVI can also occur between any rotor and any other rotor's vortices.

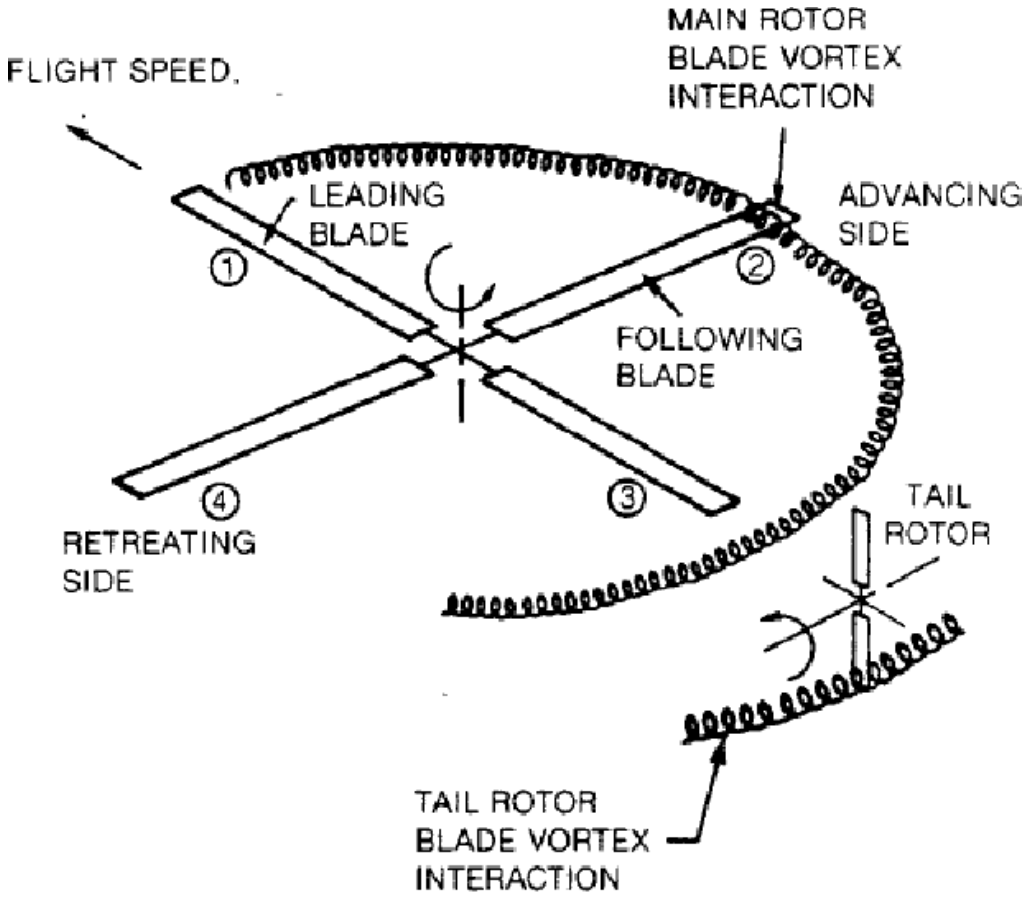

Figure 1.2: Blade-vortex interaction of a rotary wing [16]

BVI creates a significant amount of noise, especially during low-speed descent. Three different factors contribute to the production of this noise. First, the passage of the blades through or nearby the wakes of the previous blades creates intense aerodynamic noise [17] due to unsteady pressure fluctuations near the blade causing impulsive blade loading changes and, thus, vibration and sound [18]. Second, some instances of BVI occur with the blade and vortex shed from another blade parallel or nearly parallel. A two-dimensional example of this is illustrated in Figure 1.3, where the colored lines represent different blades, the black circle represents the rotor disc, the

blue cycloid represents the shed vortex from the blue blade, and the free stream velocity is to the right. Here the blades rotate counter-clockwise.

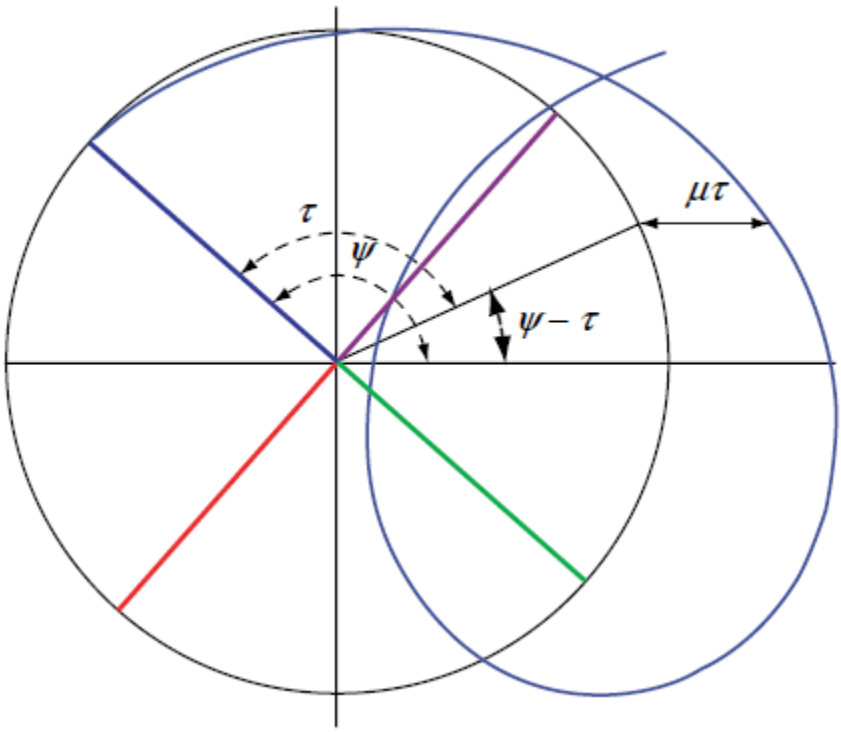

Figure 1.3: Shed vortex geometry [17]

This simplified model ignores any wake distortion effects. The cycloid is given by

$$x = \cos(\psi - \tau) + \mu\tau$$
$$y = \sin(\psi - \tau) \tag{1.1}$$

where x and y are non-dimensionalized on the rotor disc radius and x is in the free stream direction, ψ is the angle of a blade, τ is the difference in angle since the vortex at x, y was shed, and μ is the advance ratio. The advance ratio is defined as

$$\mu = \frac{V_\infty}{\Omega r} \tag{1.2}$$

where V_∞ is the free stream velocity, Ω is the rotor speed in radians per second, and r is the rotor radius. Blade-vortex intersections occur at

$$\sin(\tau - \psi_b) + \mu\tau \sin(\psi - \psi_b) = 0 \tag{1.3}$$

where ψ_b is the location of a second blade. In this instance, the purple blade is about to collide with the vortex while they are parallel. These parallel collisions occur at locations where Equation 1.3 is true and

$$\mathrm{x} = \frac{\mathrm{y}(\mathrm{y} + \mu)}{\sqrt{1 - y^2}} \tag{1.4}$$

The result is an extended-length BVI radiating in phase with high acoustic efficiency [17]. Equation 1.3 (shown in various colors corresponding to the blade colors in Figure 1.3) and Equation 1.4 (shown in yellow) are plotted within the rotor disc for various advance ratios in Figure 1.4. The intersections between the yellow curve and the other curves represents instances of parallel BVI. The third factor that contributes to high amounts of noise generated by BVI is that the change in the Mach angle (defined as the inverse sine of the reciprocal of the Mach number) of the principle acoustic radiation and the change in local angle of the shed vortex can reach a kinematic balance. This results in locally two-dimensional radiation, creating a potential for the noise field to have very localized peaks [17]. In other words, the magnitude of the sound radiated by rotorcraft as a result of BVI is not constant in all directions, but rather has some regions that are louder and others that are quieter.

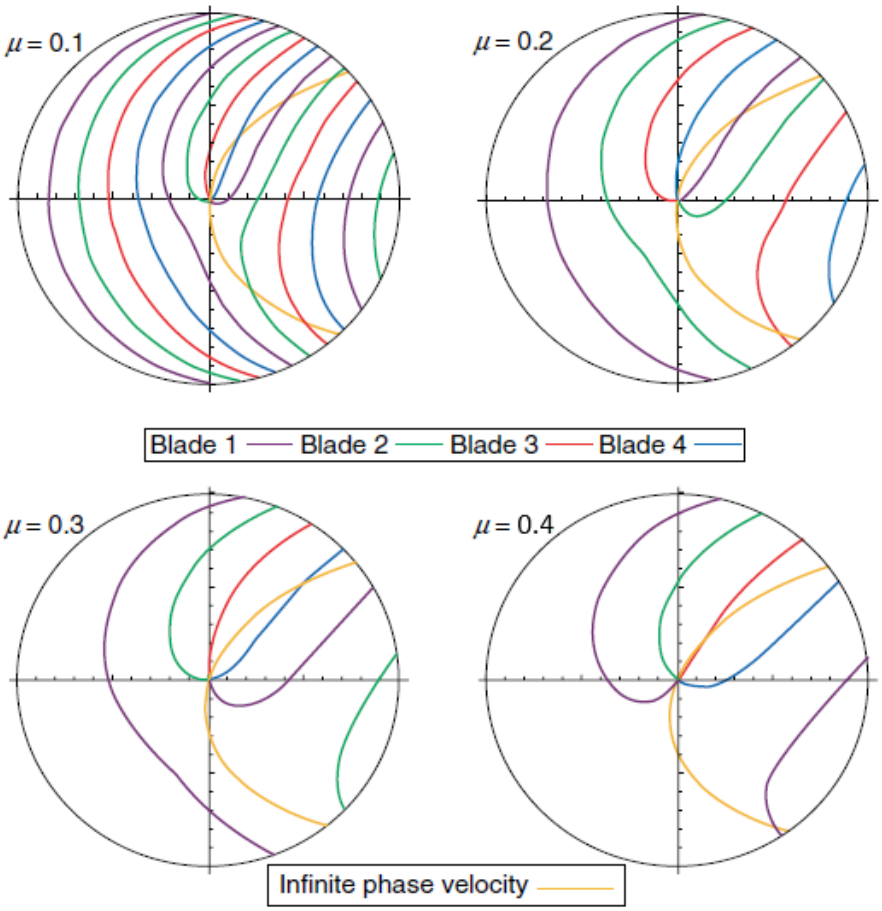

Figure 1.4: BVI locations for various advance ratios

A number of methods to reduce BVI noise have been investigated, primarily via experimental means. Some research has proven that changes to blade tip geometry can produce significant results. One such study observed a 13.5 dB reduction in the negative impulse peak pressure and up to a 5 dB reduction during low-speed descent [19]. The use of vane tip shapes alongside sweep, taper, twist, and dihedral design parameters and a discontinuous trailing edge has been shown to reduce BVI noise by 5.6 dBA while maintaining proper control loads and performance [20]. Active blade control can also be used to reduce rotor vibratory loads and mitigate BVI noise. A higher-harmonic control concept, which works by exciting a pitch angle through a rotor swashplate in all blades simultaneously at a fixed frequency, has been shown to be able to reduce BVI noise by approximately 6 dB [21]. Another concept, studying the analytical

feasibility of an active blade twist design, predicted noise reductions of 2-4 dB for strong BVI cases and 7-10 dB for weak cases [22].

1.3 Acoustic Data Collection

The collection of acoustic data with a focus on rotorcraft has been performed using a variety of flight conditions and equipment configurations. Many studies have chosen to capture acoustic data during a hover condition [23, 24]. This can be accomplished by allowing a vehicle to freely hover or by attaching a vehicle, rotor, or set of rotors to a fixed stand. Acoustic behavior under a hover condition is often simpler in nature, as the lack of movement can reduce temporal and directionality considerations, and can serve as a good starting point for observing the acoustic signature of a rotor or vehicle. The use of a fixed stand can also allow for other flight conditions to be studied in a very controlled and predictable way. For instance, one study utilized a stand so that rotor acceleration and deceleration cases could be studied without having to worry about the vehicle moving [25]. Other studies utilize one or more microphones in various fixed locations as a vehicle performs a flyover, takeoff, approach, or other maneuver [26]. Having multiple microphones set up in different locations can help to gain a good idea of the directionality of the sound, something that is very important for many rotorcraft whose sound profiles vary strongly with direction. Some studies perform acoustic data collection inside wind tunnels, some large enough to fit entire helicopters. This allows for the simulation of flight conditions with microphones at positions fixed relative to the vehicle that would not otherwise be feasible. One study used this method to capture acoustic data of a helicopter in descent conditions while remaining physically in place [27]. Another study was able to perform similar tests, however, while still having a freely moving helicopter. This was made possible by mounting microphones to a

long boom attached to the bottom of the vehicle, resulting in fixed microphone positions within the vehicle's frame of reference [14].

It is important to recognize that BVI noise is highly directional and varies dependent on not only the geometry of the aircraft but also the flight conditions. It is well understood that the strongest BVI noise is generated during descent [14, 26, 27], with mild descent cases between approximately 5.5° and 7.5° seeming to have the strongest BVI contributions [14]. This is fairly intuitive, as the flight path and direction of flow (the direction the shed vortices are being pushed) are similar. Thus, the vortices remain very close to the blades and strong BVI occurs. Conversely, cases of ascent tend to have very low BVI noise [14, 27]. BVI noise appears to radiate most strongly downwards and forwards of the vehicle in the case of helicopters, between 40° and 55° below the rotor disc, with particularly strong contributions on the advancing side of the rotor disc [14, 28]. Stronger advancing side BVI seems to concur with the presence of more BVI and parallel BVI locations on the advancing (upper) side of the plots in Figure 1.4.

The testing environment is also a significant factor to consider when planning to record acoustic data. Outdoor settings are easier to use for large vehicles, and most large open areas will only have one surface, the ground, off of which sound can echo. The outdoors, however, can sometimes offer uncontrollable background noises such as those of wildlife, weather, or human activity. Indoor settings are typically quieter, but echoes off of any interior surfaces are a major concern. This can be avoided by using an anechoic chamber, a room designed to absorb reflections of acoustic waves completely, but these are expensive to construct and existing ones are not always accessible to everyone.

1.4 Current and Future Work

If BVI and its contribution to the total noise produced by rotorcraft can be better understood, new wing and rotorcraft designs can be created to target and reduce it, aiding in the expansion of rotorcraft usage. There is much yet to be understood about BVI and the noise it produces, and the complexity of BVI makes it difficult to model and predict. Nevertheless, it can be done. Several computational models have been developed to predict noise produced by helicopters during maneuvers where BVI is prevalent, such as descent, with good accuracy [29-31]. Computational noise models have also been created for UAVs, typically focusing on quadrotors, though these seem to be less well-developed at the moment [32, 33]. Multirotor UAVs also introduce an additional level of complexity and potential for strong BVI noise in the increased number of closely-spaced rotors relative to some other rotorcraft, like helicopters. Significant work has been done to research the reduction of BVI noise, as referenced in Chapter 1.2 [19-22], but much remains to be understood.

1.5 The Decibel

In acoustics, the decibel (dB) is a unit of measurement used to quantify the intensity of sound on a relative, logarithmic scale. Because decibels are relative, any magnitude of sound can be used as a basis. Normally, the threshold of human hearing, the minimum level of sound a typical human can hear with no other noises present, is chosen to be 0 dB. This is equivalent to a sound pressure level of 20 μPa. Other magnitudes of sound are then scaled up or down logarithmically from this decibel value. For instance, a sound 10 times louder than the threshold of human hearing would be 10 dB, and a sound 100 times louder than the threshold of human hearing would be 20 dB. If a sound is quieter than the threshold, it would have a negative decibel value.

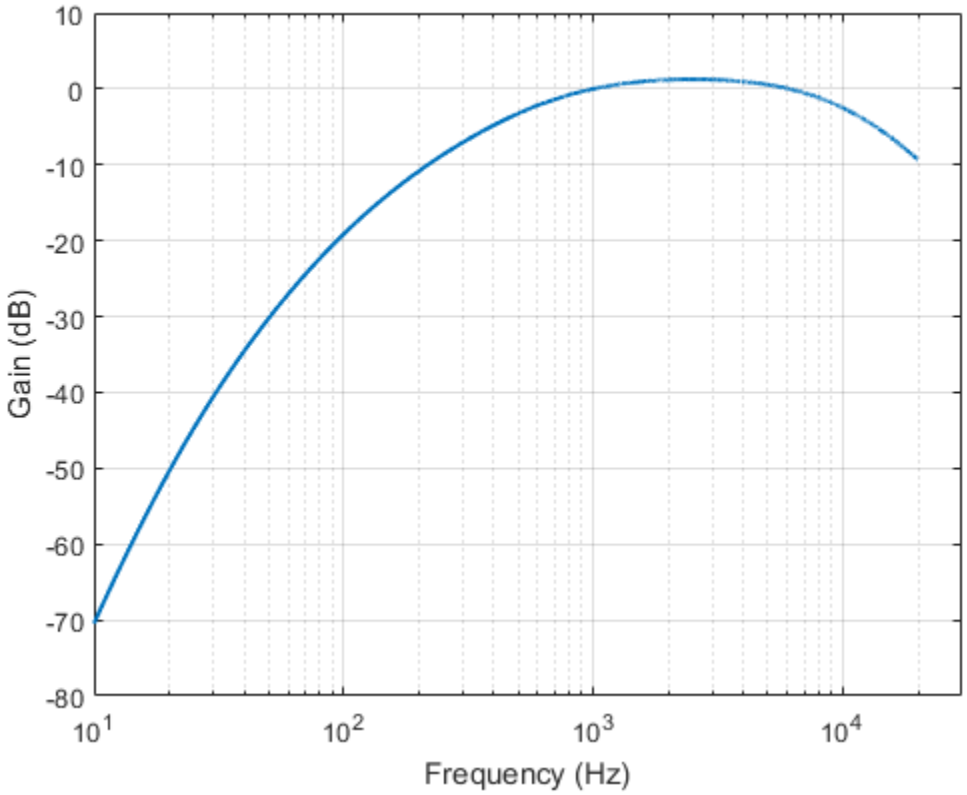

Figure 1.5: Decibel A-weighting function

There are several different ways to represent decibels outside of the choice of reference point, sometimes in the form of different weightings. A-weighted decibels (dBA) is one of the most common weighted forms of the unit because it more closely matches the human perception of sound, which is not very good at picking up low frequencies. It does this by applying a gain that varies with the frequency of the original noise. The gain function [34] can be approximately described as

$$\mathrm{A(f)} = 2.0 + 20\log_{10}\big(Ra(f)\big) \tag{1.5}$$

where

$$Ra(f) = \frac{12200^2 * f^4}{(f^2 + 20.6^2)(f^2 + 12200^2)\sqrt{(f^2 + 107.7^2)(f^2 + 737.9^2)}} \tag{1.6}$$

This gain function is depicted in Figure 1.5. With this weighting, noises with a frequency of 1000 Hz are unaffected, while lower frequencies receive an increasingly negative dB gain. Frequencies just above 1000 Hz receive a very small positive gain until about 6000 Hz, where the gain decreases into small negative values. Another important form of decibels is effective perceived noise (EPNdB). This measure is specifically designed to quantify the effects of a particular aircraft's noise on humans, and is determined by several factors. The instantaneous perceived noise level, corrections for spectral irregularities, and duration are all taken into account when calculating EPNdB, as detailed in Title 14 CFR Part 36 [9].

1.6 The Fast Fourier Transform

The form of the raw acoustic data collected for this paper was a list of voltage values and the times at which each was observed by a microphone. For many acoustic analyses, data represented in the time domain, such as these, are not particularly useful. Instead, data in the frequency domain are desired as this allows the observer to easily identify and compare the magnitudes and frequencies of peaks. The discrete Fourier transform (DFT) can be used to solve this. The DFT is defined by

$$X_k = \sum_{m=0}^{N-1} x_m e^{-\frac{2\pi i}{N} mk}, \qquad k = 0, 1, \dots, N-1 \tag{1.7}$$

where the set x_m of length N (in this case, the time domain data) is transformed into the set X_k (in this case, the frequency domain data) [35]. The fast Fourier transform (FFT) uses an algorithm to perform a similar computation at drastically increased speeds. In essence, it accomplishes this by performing several smaller DFTs rather than one large one, which is quicker because the computation time scales with the square of N. A full explanation of the underlying mathematics can be found in the paper by Nussbaumer [35].

CHAPTER 2: METHODS

In this chapter, the data collection apparatus, including the tools and devices utilized, will be discussed. Data collection and processing methods will also be detailed.

2.1 Apparatus

Acoustic data collection was performed in a radio frequency (RF) anechoic chamber at the Electromagnetics Laboratory at the University of Illinois at Urbana-Champaign [36]. While the chamber was designed specifically for electromagnetic experiments rather than acoustic ones, personal observations determined its anechoic properties to be considerably more effective than a typical indoor space and the best option available to the author and his associates. Later examination of acoustic data would also support this conclusion. Thus, the anechoic chamber was deemed a suitable location for data collection. Figure 2.1 depicts the interior of the anechoic chamber while the equipment was being set up. The chamber's ceiling and floor were made of concrete and its walls metal. Each interior surface was covered with tightly packed 2-foot-tall foam pyramids with square bases approximately 8" in length. The chamber was approximately 29' long, 12' wide, and 12' tall. The height of the pyramids occupied 2' of space on each side of the room, resulting in an effective empty space that was approximately 25' long, 8' wide, and 8' tall. The pyramids could be removed in 2-foot-square sections to allow space for equipment, walking around the floor of the room, and the insertion of elevated walking platforms which can be seen in the middle and right side of Figure 2.1. A small hole in one of the walls of the chamber was used to pass cables through while keeping the door to the chamber closed.

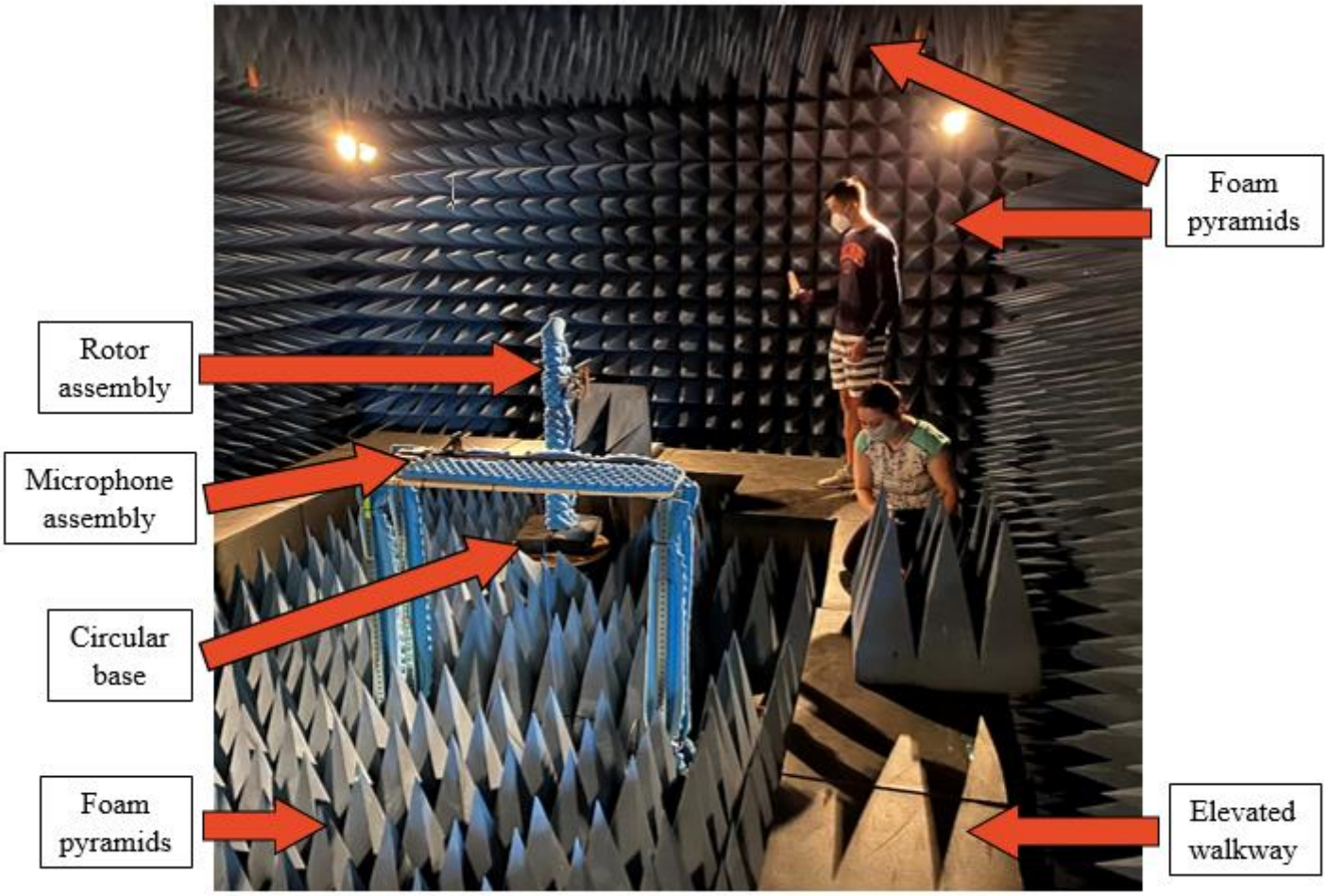

Figure 2.1: Anechoic chamber at the Electromagnetics Laboratory

The large size of the anechoic chamber provided ample space for all the acoustics equipment. This eliminated any concerns of the surfaces of the room producing any unwanted interferences with the noise and flow produced by the rotor. The data collection apparatus was positioned in the center of the chamber and is shown in Figure 2.2. The rotor, shown on the right of Figure 2.2, was powered by a Hacker A60-7XS V4 28-Pole motor and a Keysight N5700 Series DC power supply and controlled by a Castle Creations Phoenix Edge 130 electronic speed controller. The assembly was mounted to a Tyto Robotics Series 1580/1585 test stand and secured to a 4’ aluminum mounting post which was fastened to the circular base shown at the bottom of Figure 2.1 using six bolts. This left approximately 5’ of empty space between the back of the rotor

and the tips of the pyramids on the back wall of the anechoic chamber, shown in the center of Figure 2.1. The post was designed with the ability to adjust the height of the rotor, allowing for easy vertical alignment of the rotor and microphone approximately 4’ above the ground. The propeller blades were mounted to a VarioPROP 16D 2-blade propeller hub which was balanced using lead tape. All the propellers used an Eppler E387 airfoil, had a root chord of 2.25”, and had a taper ratio of 2. The propellers each had a root-to-tip span of 7.82”, and the additional space occupied by the hub caused the total rotor disc radius to be 9”. Two different sets of propellers with these characteristics were used in the data collection. The first type of propeller was designed to have a thrust coefficient of 0.003 and an optimal power requirement. The second propeller type was designed to have the same thrust coefficient and reduce the coherent tip vortex roll up in the wake near field. This difference was produced by changing the propellers’ twist distribution as determined by a cost function constrained by a specified overall root bending moment and thrust coefficient and optimized for induced torque of the system. The propeller blades were 3D-printed from ABS-M30 plastic using a fused deposition modelling process. The process used 100% infill with the blades oriented with the leading edge against the build plate during printing. After printing, the blades were sanded smooth.

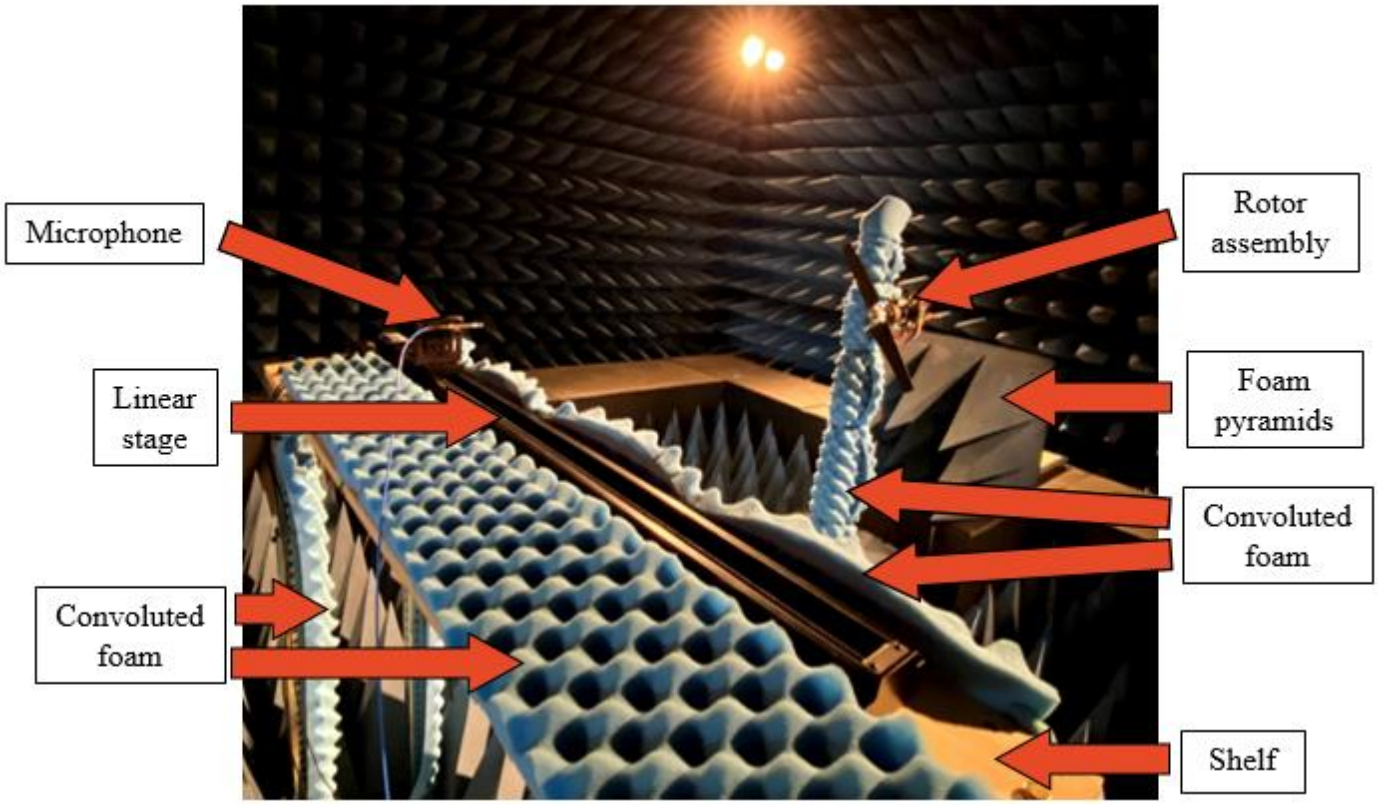

Figure 2.2: Data collection apparatus in the anechoic chamber

The microphone used, shown on the left of Figure 2.2, was a PCB model 378C01, which was comprised of a 426B03 preamplifier and a 1/4" 377C01 prepolarized microphone. It had a sensitivity of 2 mV/Pa and a frequency range of 4 Hz – 80 kHz. The microphone was connected to a PCB Piezotronics model 480C02 battery-powered signal conditioner via a 10-32 to BNC cable. The signal conditioner was connected via a BNC cable to a National Instruments PCI 6281 Data Acquisition (DAQ) device outside the chamber, which was hooked up to a computer via an SHC68-68-EPM cable. The microphone was mounted to a Zaber model X-LRT0750BL-C linear stage, shown in the center of Figure 2.2, which was placed on an elevated shelf with the actuation direction perpendicular to the rotor axis. The stage had a travel range of 750 mm (29.5 in), a resolution of 0.49609375 μm (0.019531261 mil), and an accuracy of 188 μm (7.40 mil). The stage was positioned such that the microphone was pointed directly toward the rotor and in the rotor axis

45” in the downwind direction while the stage was unactuated, as shown in Figure 2.3. A USB cable connecting the stage to the computer outside the chamber allowed for it to be controlled remotely during the data collection process. To help mitigate any acoustic reflections off the equipment, convoluted foam was fastened to the shelf and the rotor stand, and a set of foam pyramids, seen on the right of Figure 2.2, was placed on the elevated walkway directly behind the rotor.

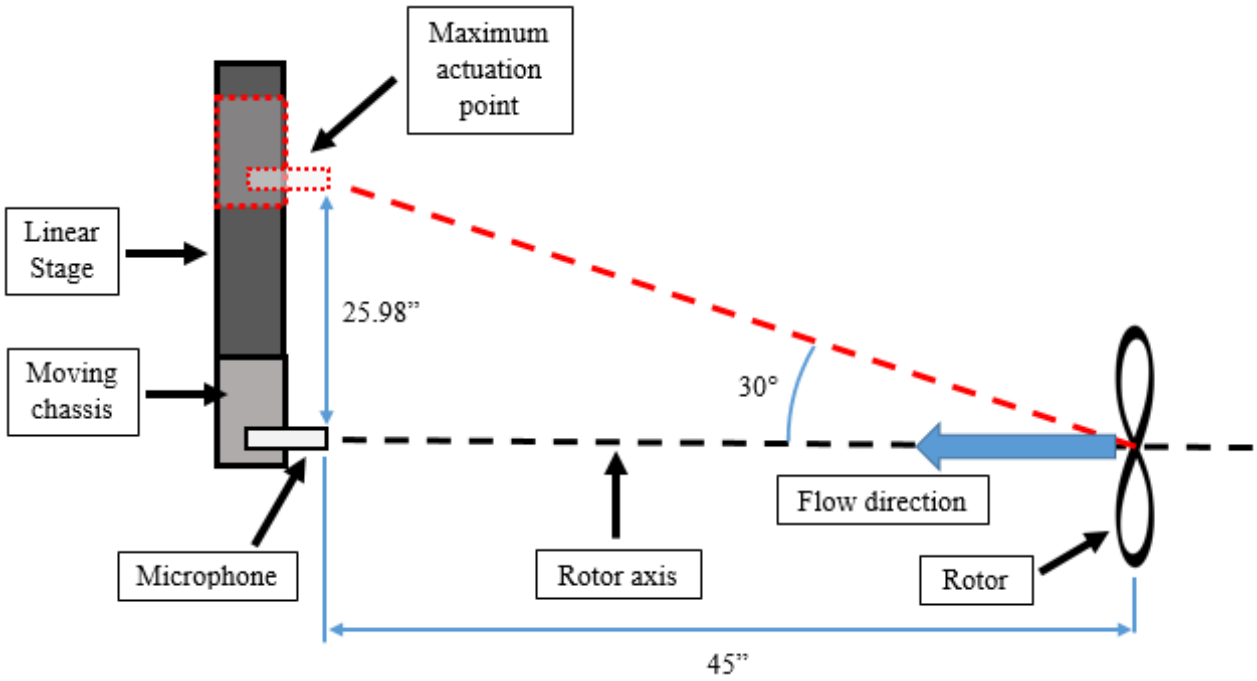

Figure 2.3: Top-down illustration of the rotor, linear stage, and microphone placement

2.2 Data Collection

Acoustic data collection was performed using the microphone at a frequency of 40 kHz with the rotor held steady at 5000 RPM for a period of 20 seconds for each test case. The microphone was actuated by the linear stage to 11 discrete locations for data collection. The locations ranged from 0º to 30º angles between the rotor axis and a line between the microphone and the rotor hub, at evenly spaced angles (one location per 3º). This resulted in a maximum linear actuation distance of 25.98”, as shown at the top of Figure 2.3. The locations are compiled in Table

2.1. Data were collected at each of these 11 locations for four sets of conditions. The first set of conditions was with background noise only and no rotor operation. The second was with the motor running at 5000 RPM with no propellers attached. The third and fourth were with each of the two propeller types with the rotor held at 5000 RPM. A simple LabVIEW program was written to save the data for each scenario into a text file.

Table 2.1: Data collection locations

Location Number	Rotor Axis Angle (deg)	Rotor Axis Distance (in)
1	0	0
2	3	2.358
3	6	4.730
4	9	7.127
5	12	9.565
6	15	12.06
7	18	14.62
8	21	17.27
9	24	20.04
10	27	22.93
11	30	25.98

2.3 Data Processing

After collection, data were processed using MATLAB. The form of the raw data was a list of voltage values and the times at which each was observed by the microphone. In order to convert the data into a more usable form, a fast Fourier transform (FFT) was performed on each data set. Next, the data were converted to decibels using Equation 2.1, where SPL is the sound pressure level in decibels, V_{rms} is the raw microphone signal in volts, S is the sensitivity of the microphone, and P_{ref} is the threshold of human hearing, which is 20 μPa.

$$SPL = \left(20Log\left(\frac{V_{rms}}{S\,P_{ref}}\right)\right) dB \tag{2.1}$$

CHAPTER 3: RESULTS

Background noise recorded inside the anechoic chamber was minimal and did not vary significantly with microphone location. Descriptions of the location numbers can be found in Table 2.1. One instance of observed background noise is shown in Figure 3.1. No distinct peaks can be seen under these conditions, and the broadband noise level sits between approximately 20 and 40 dB, about as quiet as a whisper.

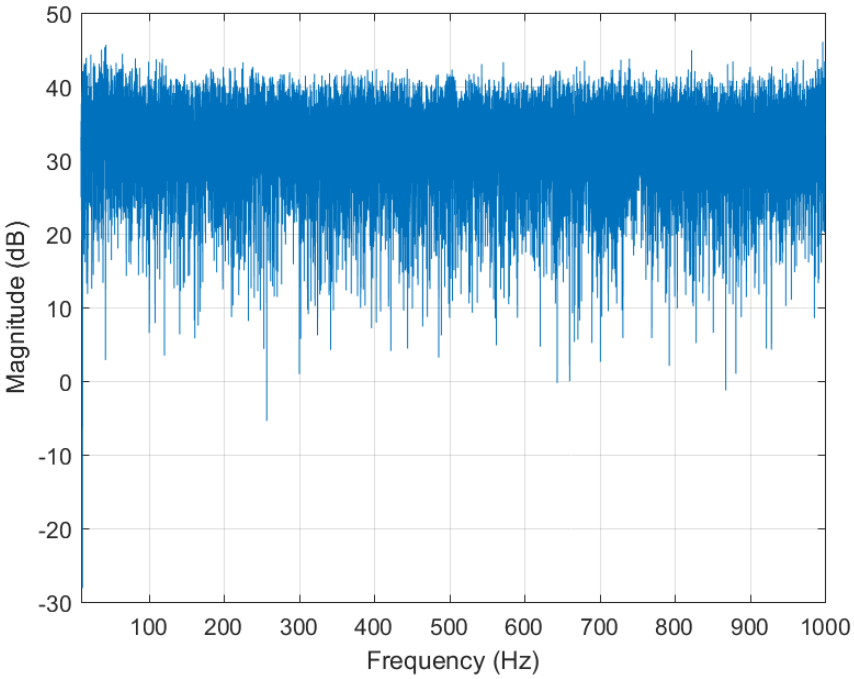

Figure 3.1: Background noise only, location 1

With the motor on and no propellers attached, little additional sound is generated, as shown in Figure 3.2. Again, no significant peaks in magnitude are seen with the exception of a very slight one just under 1000 Hz. This small peak, however, was also present in a few of the background noise cases, and thus is not likely to be due to the motor.

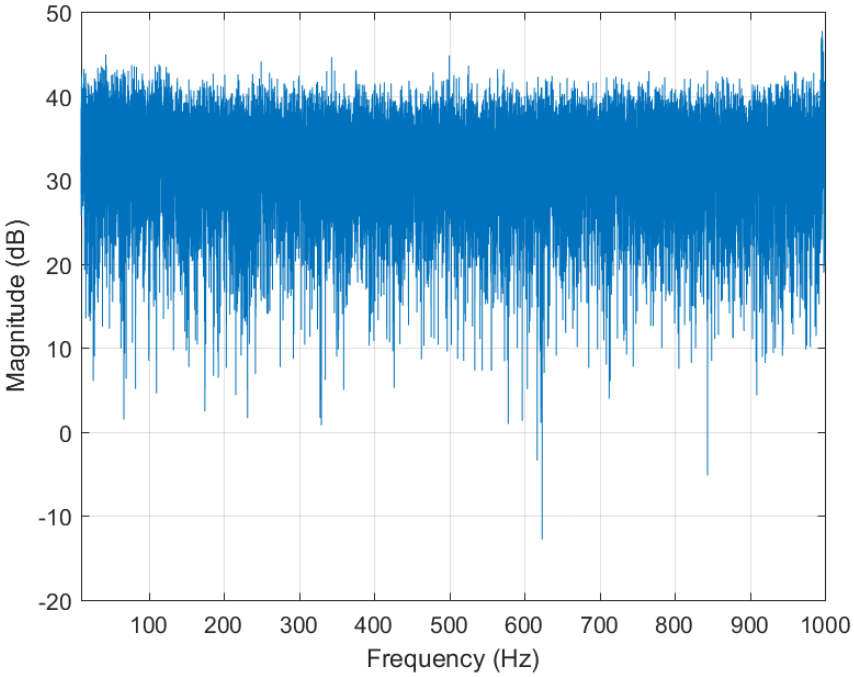

Figure 3.2: Motor noise only, location 1

With the motor on and propellers attached, the data start to vary more depending on the location. Figure 3.3 depicts the noise generated by the power optimized rotor at four different microphone locations, ranging from in the rotor axis to about 23” to the side of it. More plots can be found in the Appendix. Close to the rotor axis, especially in Figure 3.3(a) and (b), the sound is dominated by broadband noise with no distinct peaks in volume. The broadband noise is large at very low frequencies, up to as high as 80 dB, and decays to approximately 10 dB louder than the background noise levels shown previously. Moving further from the rotor axis, Figure 3.3(c) and (d) show an increasingly rapid decay in large broadband noise at low frequencies. Broadband noise approximately reaches background levels at around 300 Hz for location 7 and around 150 Hz for location 10. Distinct peaks also begin to emerge as the microphone moves away from the rotor axis, as seen in the latter two subfigures. 5 or 6 peaks are present between 0 and 1000 Hz, located at 167, 334, 501, 668, and 835 Hz in both subfigures Figure 3.3(c) and (d). This even 167 Hz

frequency spacing could be due to the fact that the propeller was spun at 5000 RPM, giving it a blade pass frequency of 10,000 RPM, which is equal to 167 Hz.

(a)

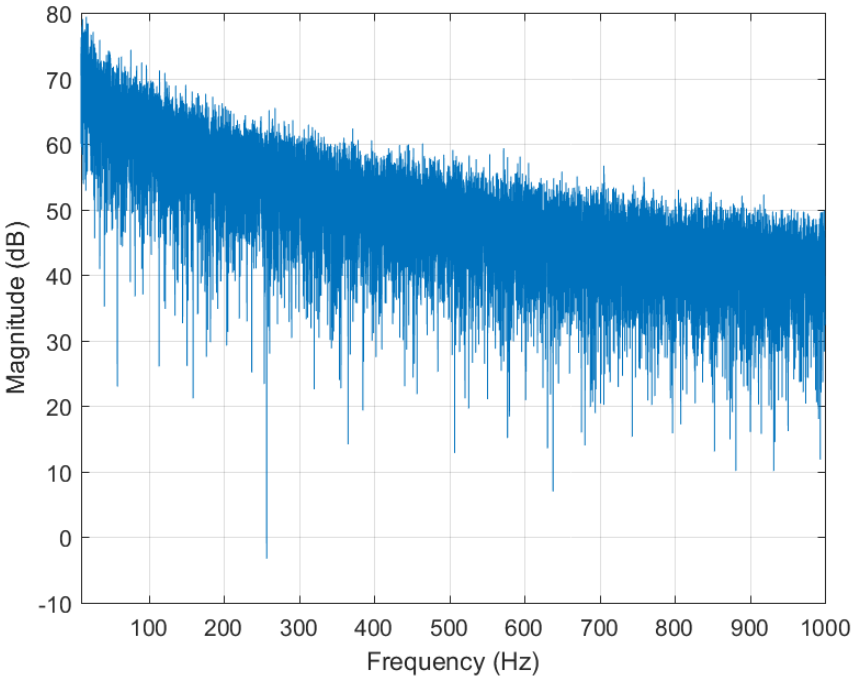

(b)

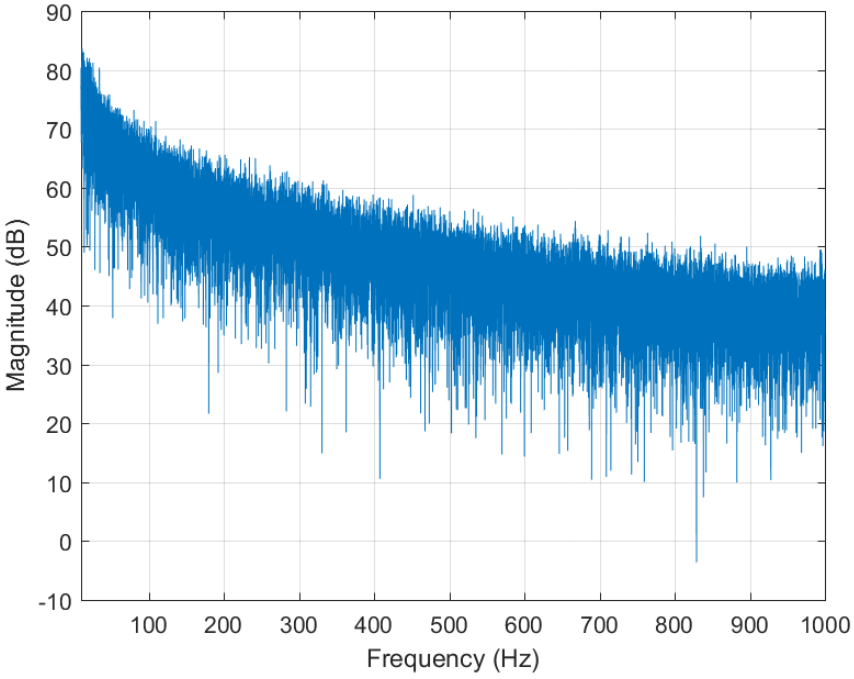

Figure 3.3 (cont.)

©

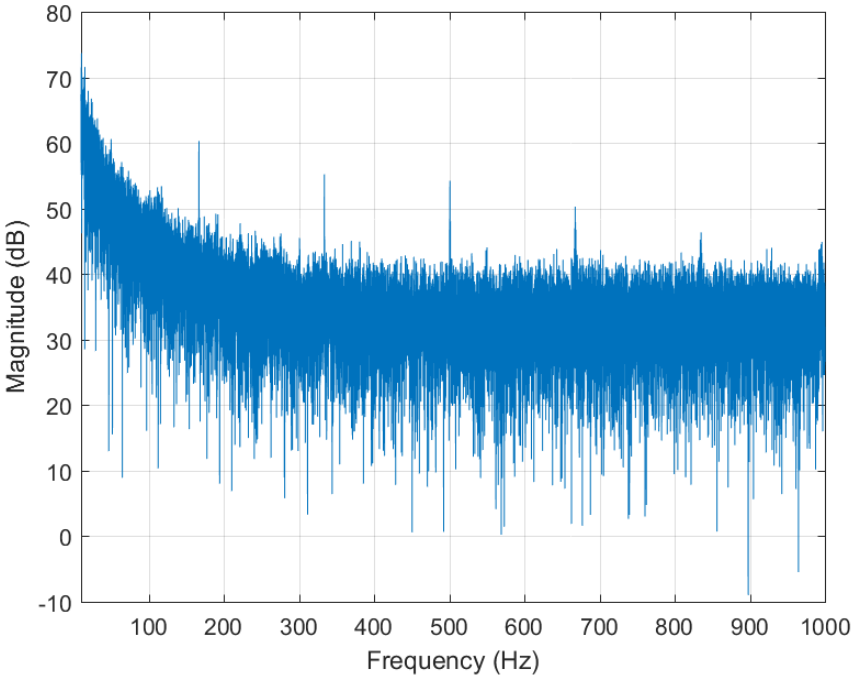

(d)

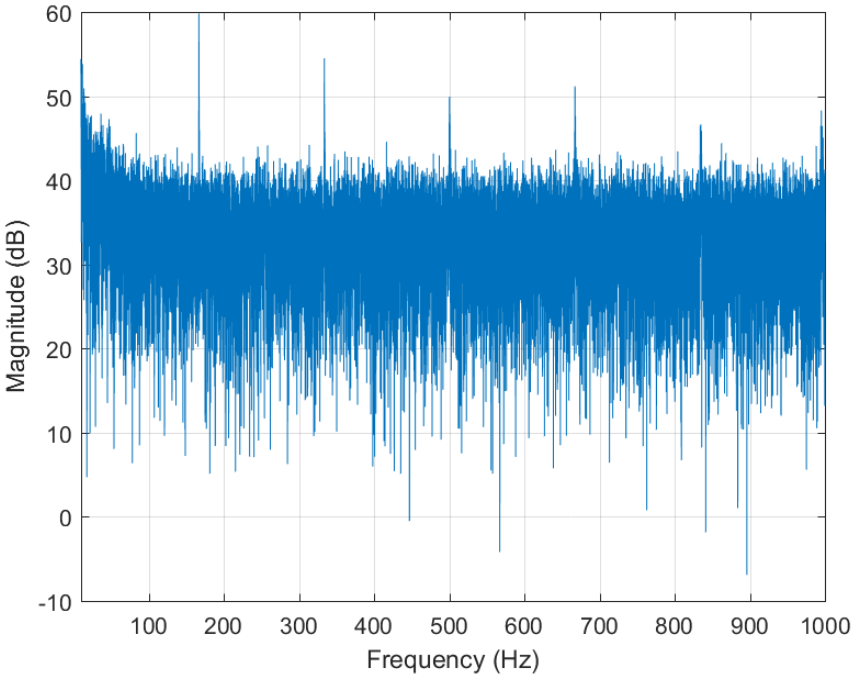

Figure 3.3: Power optimized rotor noise, locations 1 (a), 4 (b), 7 (c), and 11 (d)

Similar overall behaviors can be observed from the noise generated by the reduced vortex blades, as shown in Figure 3.4. Again, high broadband noise dominates the lower frequencies, trailing off as the microphone's distance from the rotor axis increases. Near the rotor axis, this noise is slightly greater than that generated by the power optimized blades. It maximizes at almost 90 dB at very low frequencies for locations 1 and 4, and at 1000 Hz it only decays to approximately 15 dB above background levels at location 1 and approximately 10 dB above background levels at location 4. The broadband noise once again decays toward background levels much more quickly as the microphone moves further from the rotor axis reaching this state at approximately the same frequencies as with the other rotor. Peaks also emerge in the latter two microphone positions at the same frequencies as before (167, 334, 501, 668, and 835 Hz) as well as a few new frequencies. A very prominent peak now appears at 83.4 Hz, and a weaker one appears at 250 Hz.

(a)

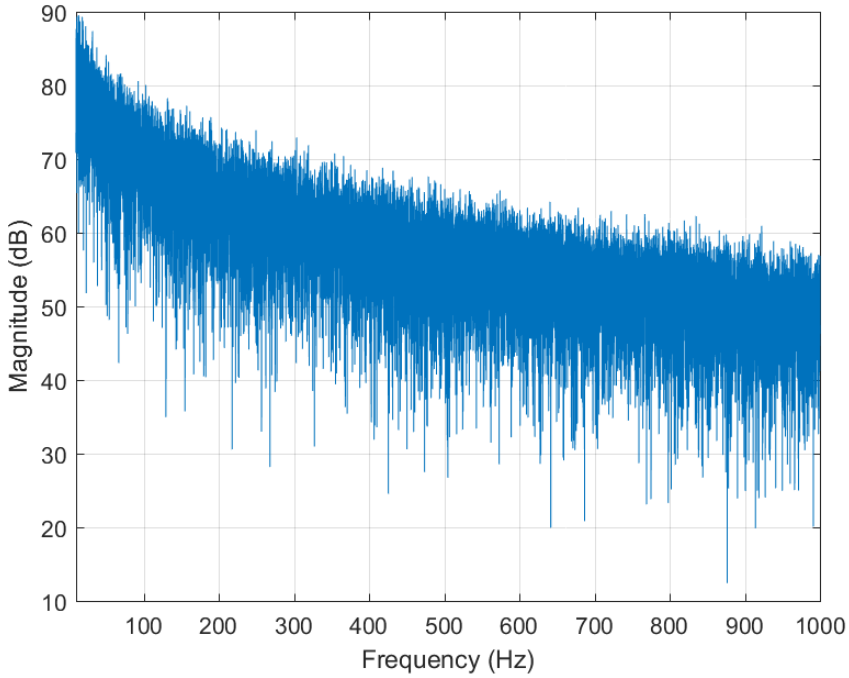

(b)

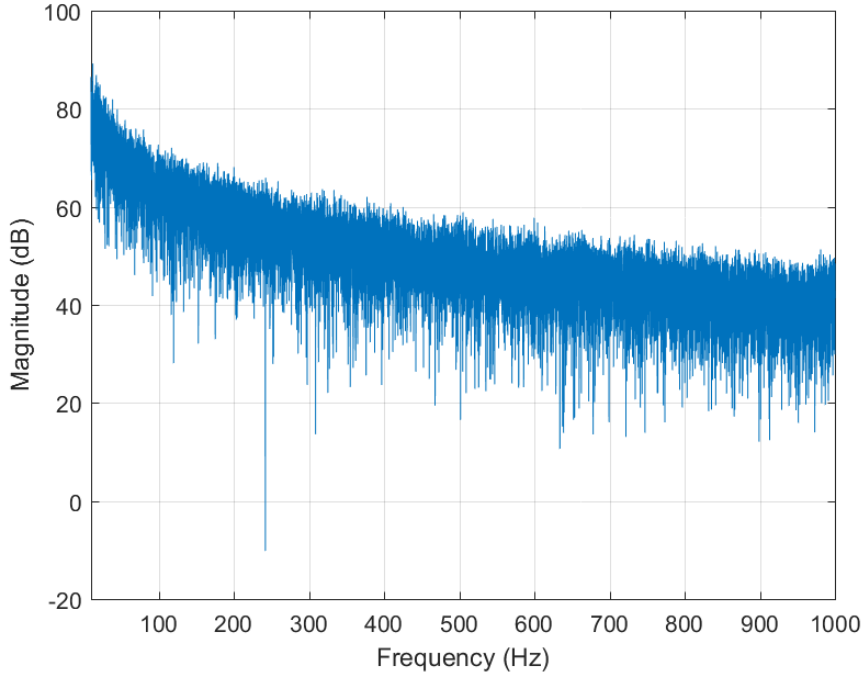

Figure 3.4 (cont.)

(c)

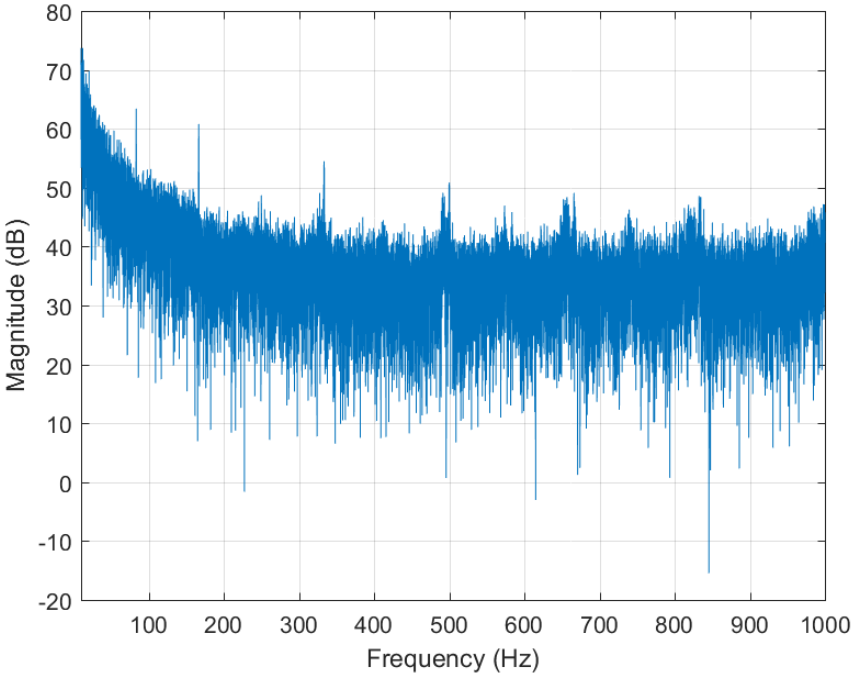

(d)

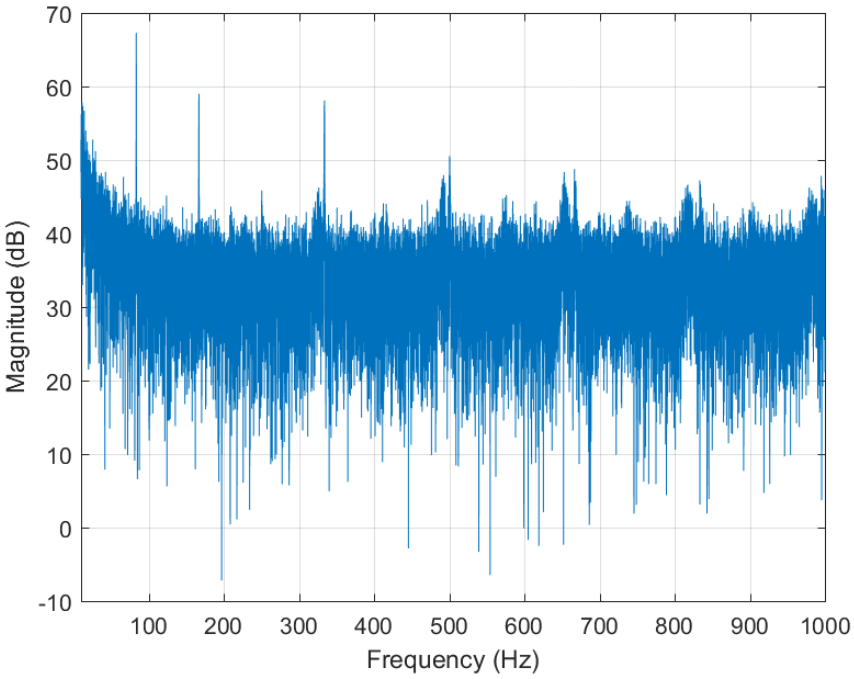

Figure 3.4: Reduced vortex rotor noise, locations 1 (a), 4 (b), 7 (c), and 10 (d)

Several simplified noise plots comparing the acoustic signature of each propeller in the same location are shown in Figure 3.5. Here, the background noise, represented by the black curve, has been smoothed using a 1000-point (50 Hz) rolling average window. Significant peaks are identified and marked by circles, where red circles are associated with the power optimized blades and blue circles are associated with the reduced vortex blades. Dashed black lines help to visually emphasize the height of each peak above the broadband noise level. As previously observed, near the rotor axis no significant peaks are present, so locations 1-4 are not included. This may be due to the fact that locations 1-4 are all within 9" (the rotor disc radius) of the rotor axis and therefore within the wake, resulting in a great amount of broadband sound. As the microphone moves further away from the rotor axis, peaks begin to emerge, being more prevalent in the higher frequencies at first. Overall, the two blades exhibit similar noise profiles. Many of the peaks are present for both blade types at frequencies within a few Hertz of one another and at similar magnitudes. However, one large difference can be observed immediately in that the reduced vortex blades resulted in a greater number of distinct peaks than the power optimized blades in all scenarios. This is especially prevalent in Figure 3.5(e), where the reduced vortex blade has 9 significant peaks under 1000 Hz while the power optimized blade has just 4. The peaks appear to be significantly greater in magnitude at low frequencies, where they can reach almost 70 dB. At around 300 Hz and higher, the peaks trail off slightly, mostly remaining between 45 and 55 dB.

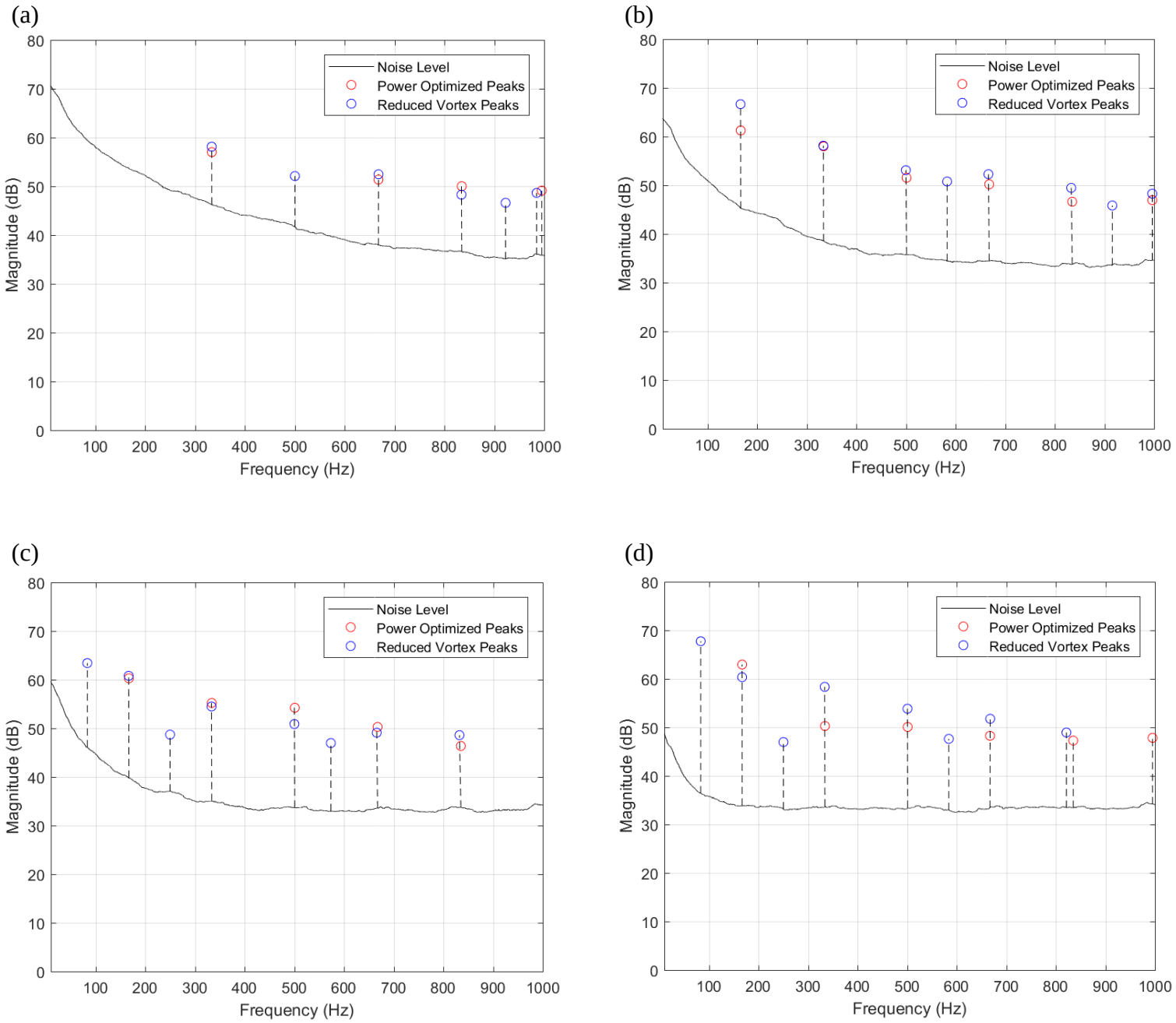

Figure 3.5 (cont.)

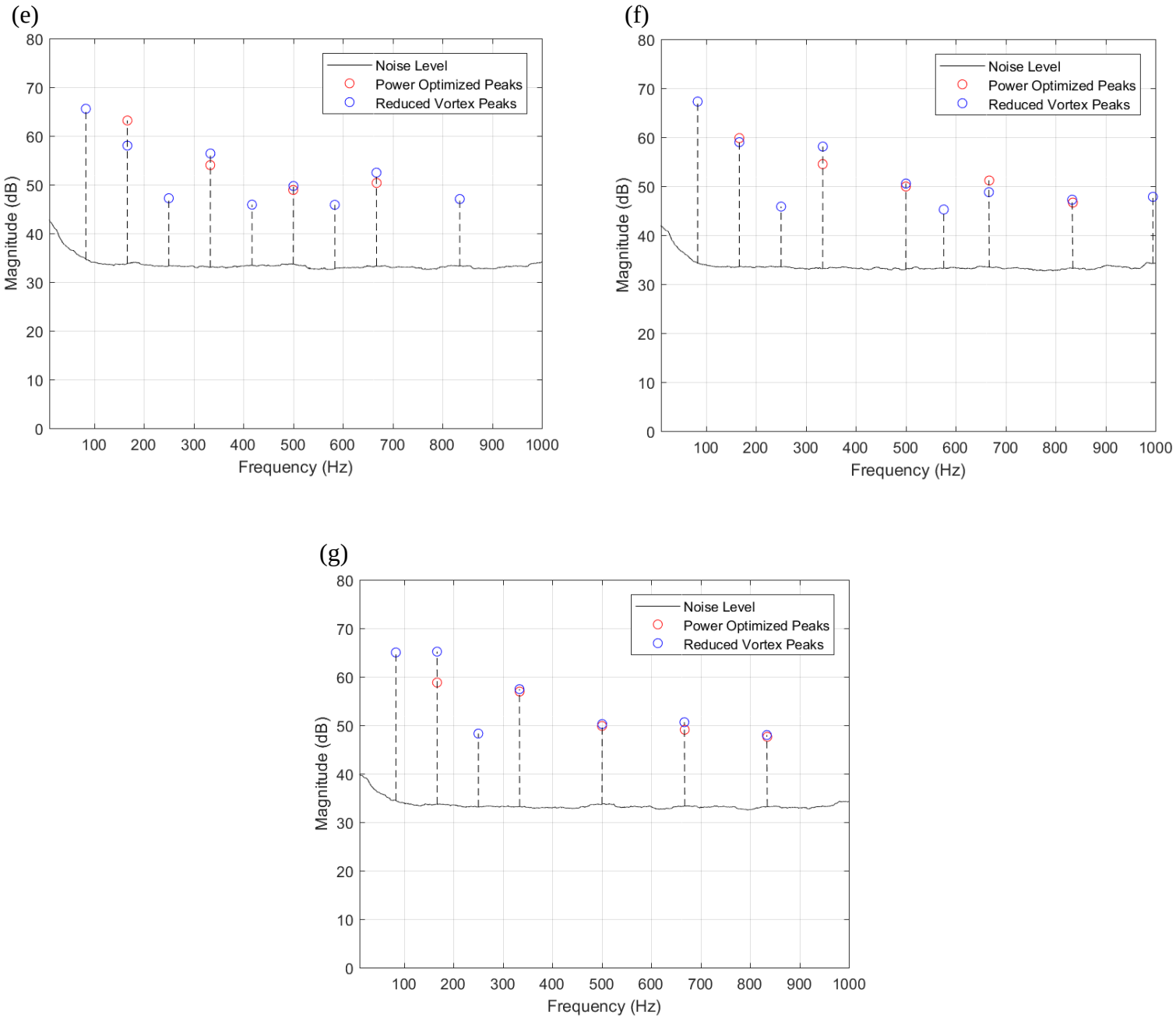

Figure 3.5: Simplified noise plots of different propeller blades under the same conditions, locations 5 (a), 6 (b), 7 (c), 8 (d), 9 (e), 10 (f), and 11 (g)

The differences in the magnitudes of peaks with matching frequency vary greatly, and it is difficult to decisively identify any strict patterns. Figure 3.6 illustrates these differences. The gain is calculated as the peak magnitude generated by the reduced vortex blades minus the peak magnitude generated by the power optimized blades, in dB. Thus, a positive gain implies that the reduced vortex blades had a greater magnitude than the power optimized blades. The overall average gain across all points is 1.09 dB, making the reduced vortex blades slightly louder even without regard to the additional peaks it has compared to the power optimized blades. The location with the greatest average gain across all frequencies is number 8 at 3.18 dB, and the location with the lowest and only negative average gain is number 7 at -0.507 dB. Beyond these averages, there are very few statistical consistencies of note. These data can be found in tabulated form in Table 5.1 in the Appendix.

The reduced vortex blades have proven to be noisier than the power optimized blades. This is true when examining peaks at frequencies where both blade types were prevalent and in a broadband perspective, as the reduced vortex blade had a greater number of significant peaks as well. At this point in time, the exact cause of this result can only be speculated. One possible explanation could be that in the breaking up of vortices that would have formed at the wing tips, other turbulent motions were created in the flow, leading to greater sound generation.

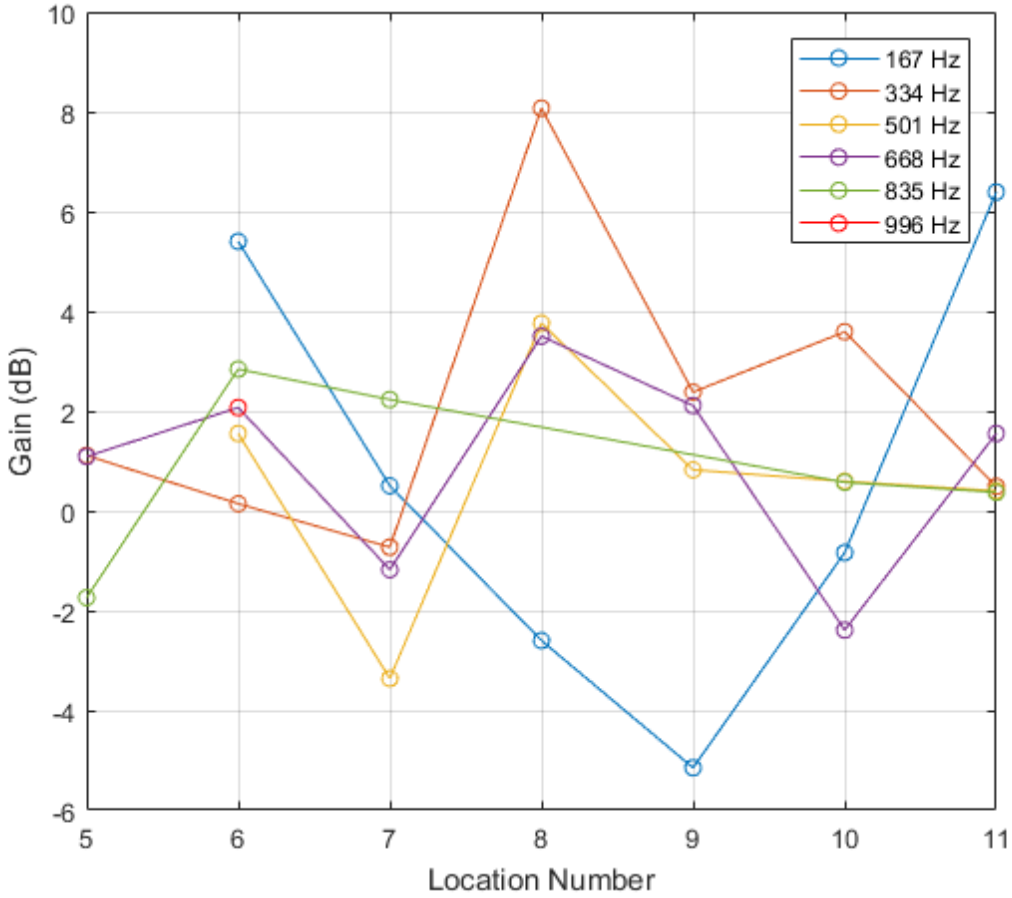

Figure 3.6: Difference in magnitude of peaks generated by the two blade types at same frequencies across different locations

CHAPTER 4: CONCLUSIONS

An acoustics data collection experiment was designed and executed for two propeller blade types, one traditional power-optimized blade and one novel reduced vortex blade. The tests were performed inside an anechoic chamber with the blades held at steady RPM. Data were collected at a handful of microphone locations, with the microphone being actuated remotely by a linear stage. Data were processed using a Fourier transform and analyzed. Key peaks in the processed data were identified for each blade type and microphone location. Compared to the traditional power optimized blade, the reduced vortex blade was found to have a greater number of distinct peaks. Additionally, for peaks that were present in the acoustic signatures of both blade types, the reduced vortex blade's peaks were slightly greater in magnitude on average. Unfortunately, these results indicate that the reduced vortex blade, which was designed in the hopes of reducing noise production via the weakening of tip vortex formation and blade-vortex interaction (BVI), was noisier than the traditional blade under the tested conditions. A definitive explanation of this result is not yet clear. One possible explanation could be that in the interruption of tip vortex formation, other turbulent flow characteristics were induced in the flow, both strengthening and broadening the sound.

Future work is necessary to fully understand the acoustic behavior of the novel blade design. Because the key purpose of the reduced vortex blade is to minimize BVI, performing further data collection in conditions where BVI is more prevalent, such as descent, could help to identify the blade's most optimal performance. Such data collection would likely require the use of either a wind tunnel or a moving apparatus or vehicle, introducing an additional layer of complexity that was beyond the scope of these initial tests. A vortex analysis of the blades, such

as through the use of particle image velocimetry, may also provide some additional explanations as to why the blades performed in the ways they did.

REFERENCES

[1] Schwindt, S., Green, D., & Duchesneau, D. (n.d.). *Drone photography basics & tips for beginners | Adobe*. Adobe. Retrieved November 17, 2021, from https://www.adobe.com/creativecloud/photography/discover/drone-photography.html

[2] Gardner, S. (2020, April 27). *Drone Racing League looks to expand "intersection of sport and technology" with groundbreaking new hire*. USA Today. Retrieved November 17, 2021, from https://eu.usatoday.com/story/sports/2020/04/27/drone-racing-league-ex-nba-exec-raises-profile-pro-sport/3026437001/

[3] Glink, I. (2017, March 7). *9 ways drones are changing real estate*. CBS News. Retrieved November 17, 2021, from https://www.cbsnews.com/media/9-ways-drones-are-changing-real-estate/

[4] *Use Cases*. (n.d.). Nightingale Security | Robotic Aerial Security. Retrieved November 17, 2021, from https://www.nightingalesecurity.com/use-cases/

[5] *Amazon.com: Prime Air*. (n.d.). Amazon. Retrieved November 17, 2021, from https://www.amazon.com/Amazon-Prime-Air/b?ie=UTF8&node=8037720011

[6] Wolfe, F. (2019, November 19). *Elbit Showcasing MAGNI Intelligence Drone at Paris Homeland Security Conference*. Defense Daily. Retrieved November 17, 2021, from https://www.defensedaily.com/elbit-showcasing-magni-intelligence-drone-paris-homeland-security-conference/advanced-transformational-technology/

[7] *Joby Aviation Welcomes New $75M Investment from Uber as it Acquires Uber Elevate and Expands Partnership*. (2020, December 8). Joby Aviation. Retrieved November 17, 2021, from https://www.jobyaviation.com/news/joby-aviation-welcomes-new-75m-investment-

from-uber-as-it-acquires-uber-elevate-and-expands-partnership/?uclick_id=a33c12f7-8e38-4dd4-8484-d3aad1a20a10

[8] Cabell, R., McSwain, R., & Grosveld, F. (2016, June). Measured Noise from Small Unmanned Aerial Vehicles. *Noise-Con 2016*, Providence, RI.

[9] Noise Standards: Aircraft Type and Airworthiness Certification, 14 C.F.R. § 36 (2021).

[10] Holden, J., & Goel, N. (2016, October). Fast-Forwarding to a Future of On-Demand Urban Air Transportation. Uber.

[11] *Joby Unveils eVTOL Design Details And Certification Plans*. (2020, September 25). Aviation Week Network. Retrieved November 19, 2021, from https://aviationweek.com/aerospace/urban-unmanned-aviation/joby-unveils-evtol-design-details-certification-plans

[12] Massey, K., & Gaeta, R. (2010, June). Noise Measurements of Tactical UAVs. *16th AIAA/CEAS Aeroacoustics Conference*, Atlanta, GA. https://doi.org/10.2514/6.2010-3911

[13] Leverton, J. W. (1971). The sound of rotorcraft. *The Aeronautical Journal*, *75*(726), 385-397.

[14] Schmitz, F. H., Greenwood, E., Sickenberger, R. D., Gopalan, G., et al. (2007). Measurement and characterization of helicopter noise in steady-state and maneuvering flight.

[15] Guha, T. K., Oates, W. S., & Kumar, R. (2015, May). Characterization of Piezoelectric Macrofiber Composite Actuated Winglets. *Smart Materials and Structures*, 065043. https://doi.org/10.1088/0964-1726/24/6/065043

[16] Schlinker, R., & Amiet, R. (1983, April). Rotor-vortex Interaction Noise. *8th Aeroacoustics Conference*, Atlanta, GA. https://doi.org/10.2514/6.1983-720

[17] Lowson, M. (2014). Acoustic Kinematics of Helicopter BVI Noise. *17th AIAA/CEAS Aeroacoustics Conference (32nd AIAA Aeroacoustics Conference)*, *14*(1-2), 229–256. https://doi.org/10.2514/6.2011-2805

[18] Malovrh, B., & Gandhi, F. (2005). Sensitivity of Helicopter Blade-Vortex-Interaction Noise and Vibration to Interaction Parameters. *Journal of Aircraft*, *42*(3), 685–697. https://doi.org/10.2514/1.4466

[19] Lowson, M. (1992). Progress towards quieter civil helicopters. *The Aeronautical Journal (1968)*, *96*(956), 209-223. doi:10.1017/S0001924000050508

[20] Brocklehurst, A., & Pike, A. C. (1994, January). Reduction of BVI Noise Using a Vane Tip. In *AHS Aeromechanics Specialists Conference*.

[21] Polychroniadis, M. (1990). Generalized Higher Harmonic Control, ten years of aerospatiale experience. In *16th European Rotorcraft Forum, Glasgow, UK, September 1990*.

[22] Chen, P. C., Baeder, J. D., Evans, R. A. D., & Niemczuk, J. (2001). Blade-vortex Interaction Noise Reduction with Active Twist Smart Rotor Technology. *Smart Materials and Structures*, *10*(1), 77–85. https://doi.org/10.1088/0964-1726/10/1/307

[23] Kloet, N., Watkins, S., & Clothier, R. (2017). Acoustic signature measurement of small multi-rotor unmanned aircraft systems. *International Journal of Micro Air Vehicles*, *9*(1), 3–14. https://doi.org/10.1177/1756829316681868

[24] Tinney, C. E., & Sirohi, J. (2018). Multirotor Drone Noise at Static Thrust. *AIAA Journal*, *56*(7), 2816–2826. https://doi.org/10.2514/1.j056827

[25] Yang, J., & Saxton-Fox, T. (2020). Small Unmanned Aircraft Systems (sUAS) rotor acoustic noise at unsteady thrusts.

[26] Conner, D., Marcolini, M., Edwards, B., & Brieger, J. (1997, April 29–May 1). *XV-15 Tiltrotor Low Noise Approach Operations*. American Helicopter Society 53rd Annual Forum, Virginia Beach, VA, United States.

[27] Brooks, T. F., Jolly, J. R., Jr., & Marcolini, M. A. (1988, August). *Helicopter Main-Rotor Noise: Determination of source contributions using scaled model data*. NASA. https://ntrs.nasa.gov/citations/19880017523]

[28] Martin, R. M., Marcolini, M. A., Splettstoesser, W. R., & Schultz, K. J. (1990, November). *Wake Geometry Effects on Rotor Blade-Vortex Interaction Noise Directivity*. NASA. https://ntrs.nasa.gov/citations/19910003002

[29] Bernardini, G., Serafini, J., Ianniello, S., & Gennaretti, M. (2007). Assessment of Computational Models for the Effect of Aeroelasticity on BVI Noise Prediction. *International Journal of Aeroacoustics*, *6*(3), 199–222. https://doi.org/10.1260/147547207782419570

[30] Shirey, J., Brentner, K., & Chen, H. N. (2007, January). A Validation Study of the PSU-WOPWOP Rotor Noise Prediction Code. *45th AIAA Aerospace Sciences Meeting and Exhibit*. 45th Aerospace Sciences Meeting and Exhibit, Reno, NV. https://doi.org/10.2514/6.2007-1240

[31] Greenwood, E., Rau, R., May, B., & Hobbs, C. (2015, May). A maneuvering flight noise model for helicopter mission planning. In *American Helicopter Society 71st Annual Forum*.

[32] Vieira, A., Cruz, L., Lau, F., Mortagua, J., & Santos, R. (2015). A new computational framework for UAV quadrotor noise prediction. In *5th CEAS Air & Space Conference* (pp. 1-14).

[33] Lee, H., & Lee, D. J. (2019). Numerical prediction of aerodynamic noise radiated from a propeller of unmanned aerial vehicles. *Inter. Noise 2019*, 1-9.

[34] Acoustical Society of America. (2001). *Design Response of Weighting Networks for Acoustical Measurement*. ANSI/ASA Standard S1.42-2001 (R2016).

[35] Nussbaumer, H. J. (2013). *Fast Fourier Transform and Convolution Algorithms*. Springer Publishing. https://doi.org/10.1007/978-3-662-00551-4_4

[36] Bernhard, J. (2021). *EM Lab @ UIUC*. http://antennas.ece.illinois.edu/

APPENDIX A: ADDITIONAL ACOUSTIC DATA

Some additional noise plots and other information not included in Chapter 3 are provided here.

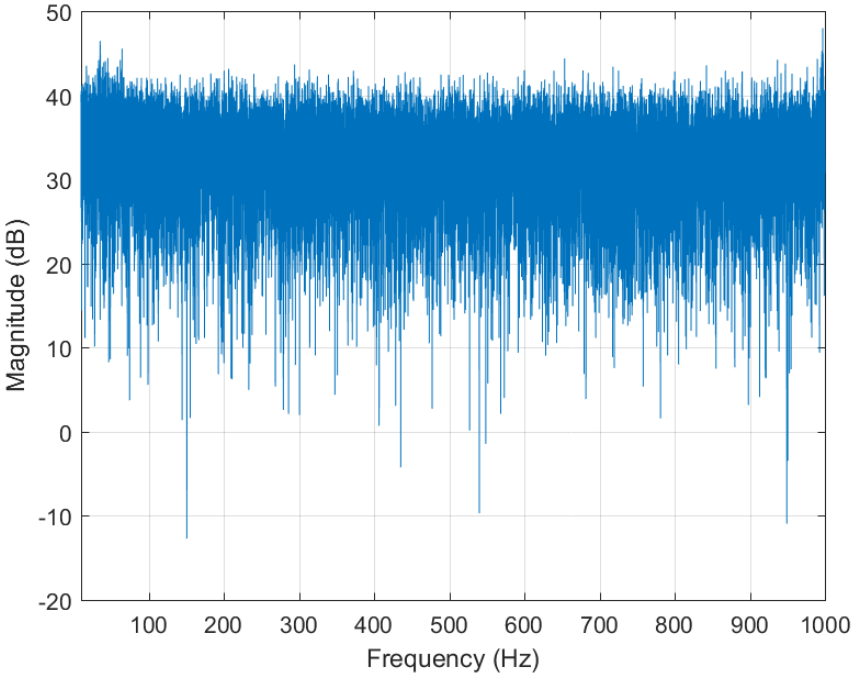

Figure A.1: Background noise only, location 4

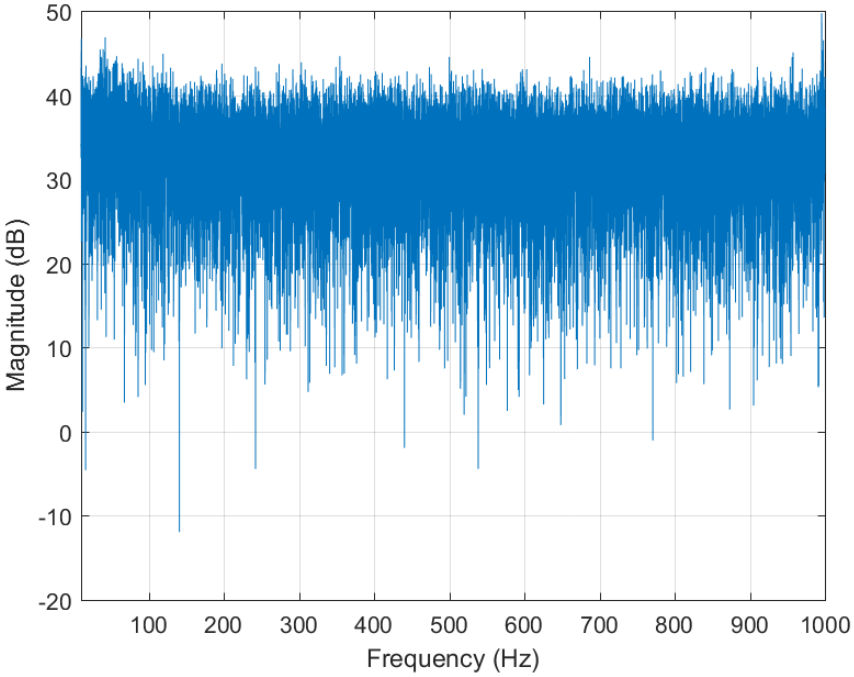

Figure A.2: Background noise only, location 10

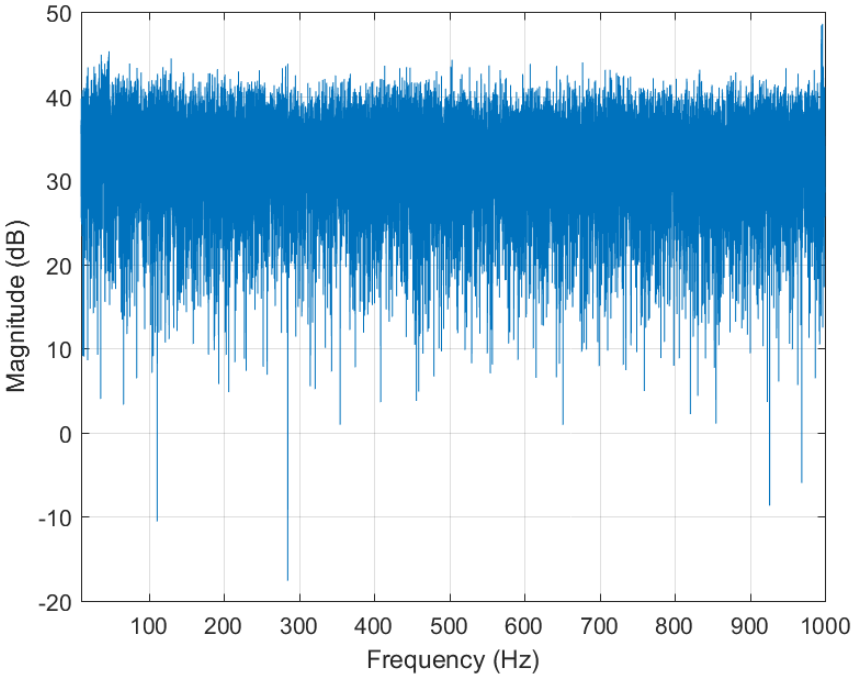

Figure A.3: Motor noise only, location 4

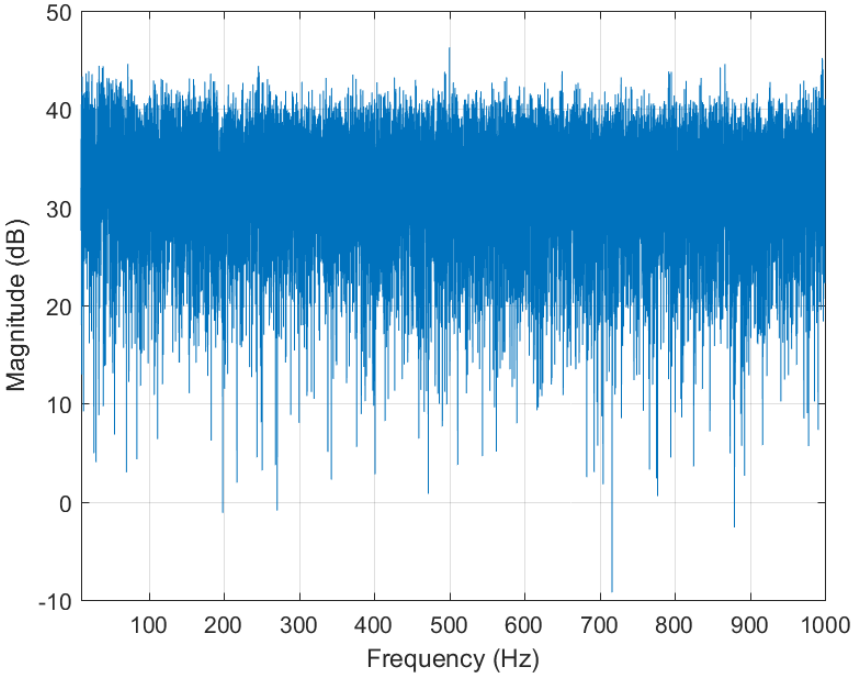

Figure A.4: Motor noise only, location 10

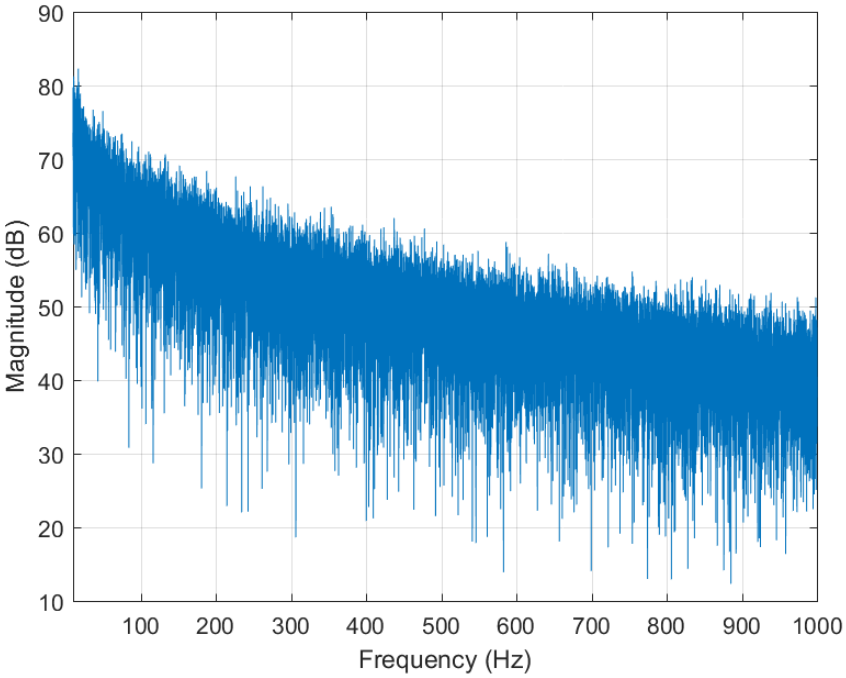

Figure A.5: Power optimized rotor noise, location 2

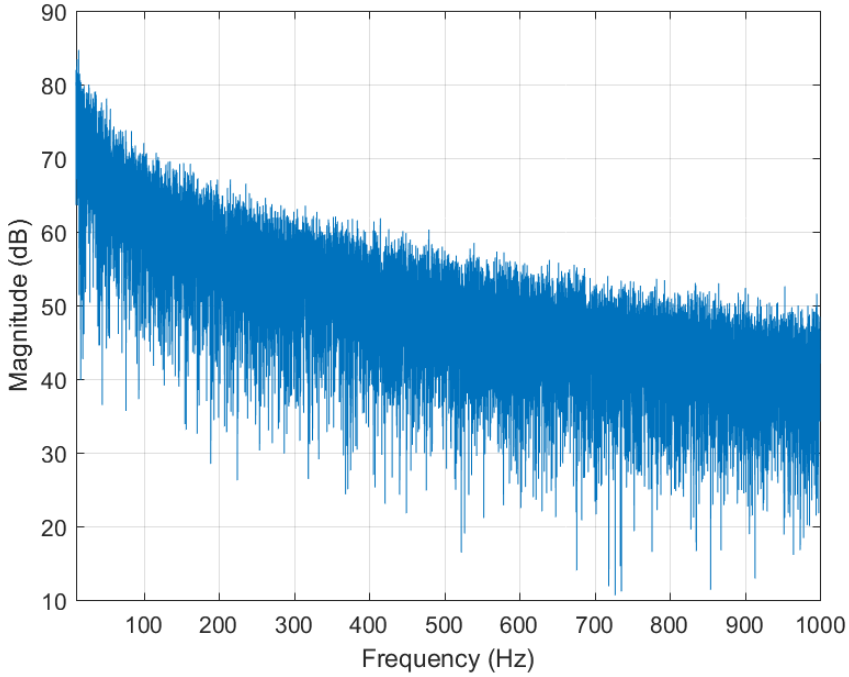

Figure A.6: Power optimized rotor noise, location 3

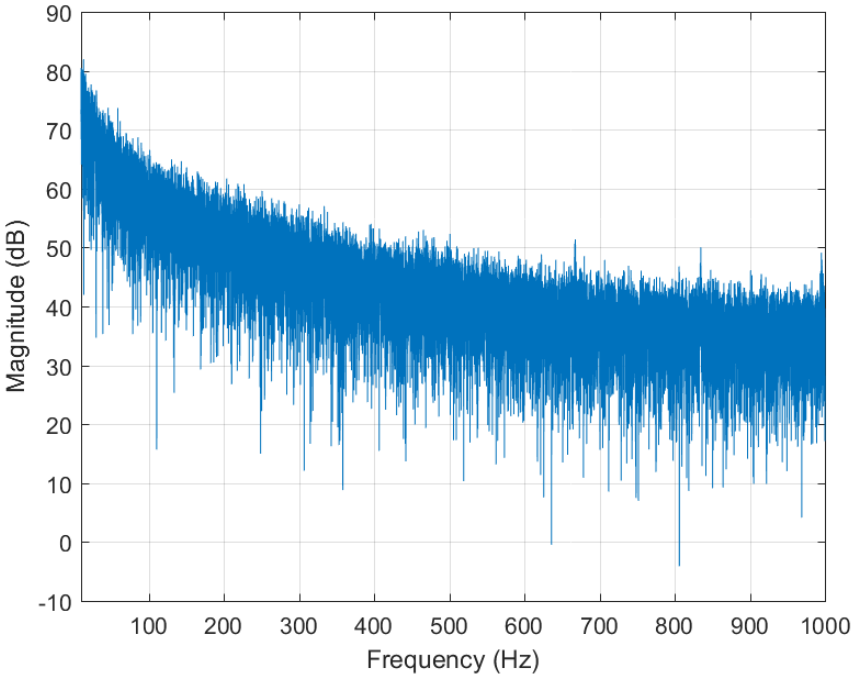

Figure A.7: Power optimized rotor noise, location 5

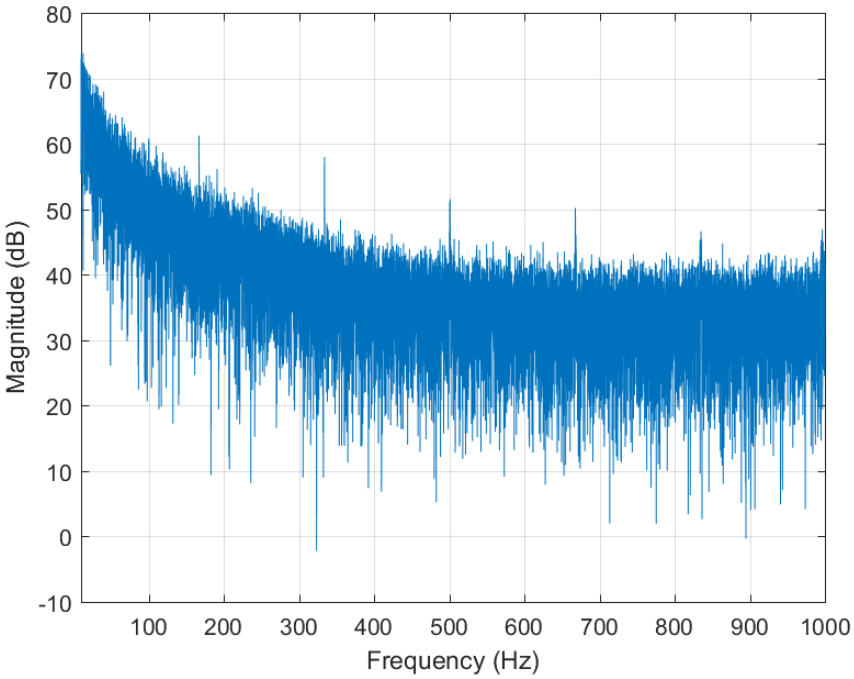

Figure A.8: Power optimized rotor noise, location 6

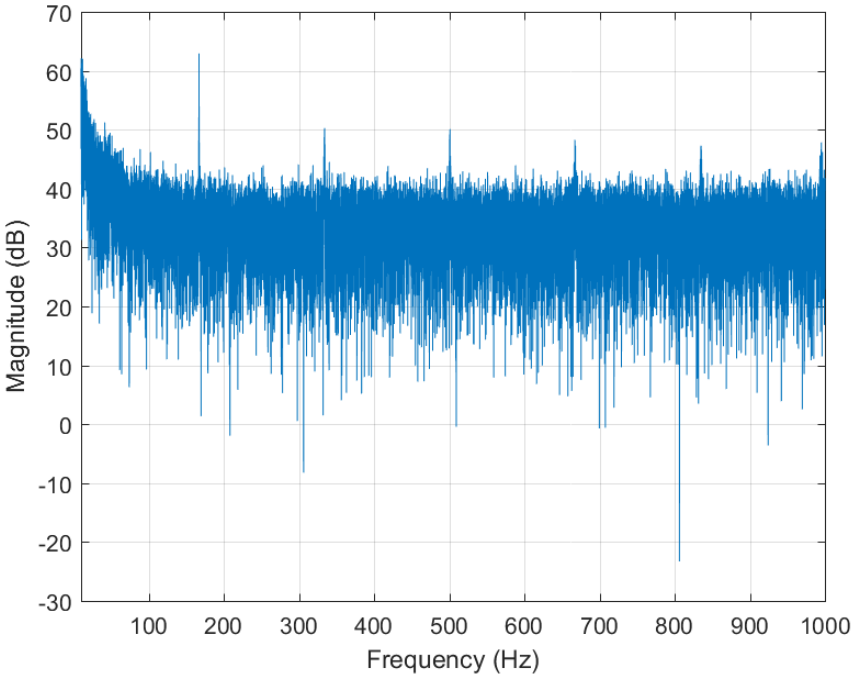

Figure A.9: Power optimized rotor noise, location 8

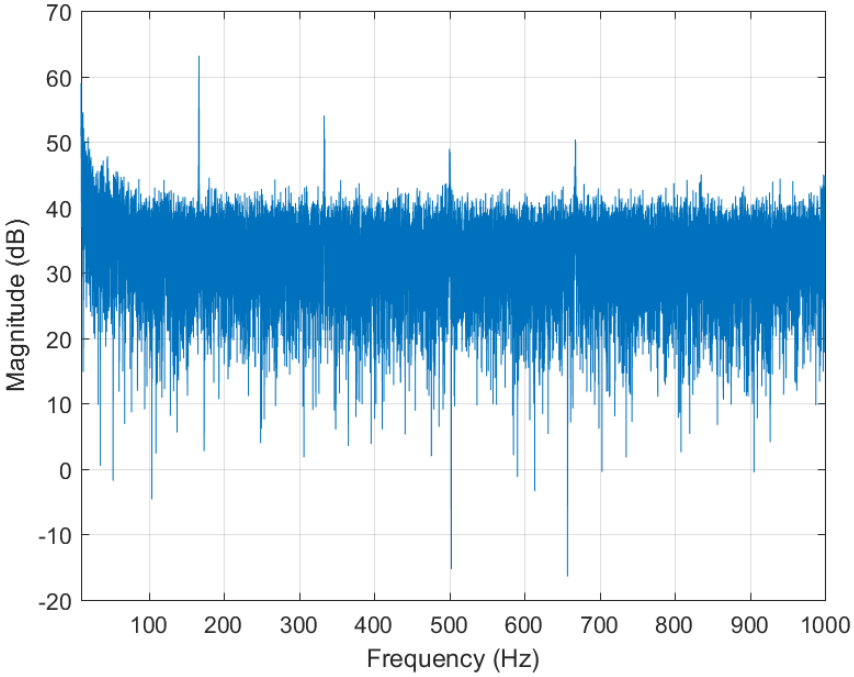

Figure A.10: Power optimized rotor noise, location 9

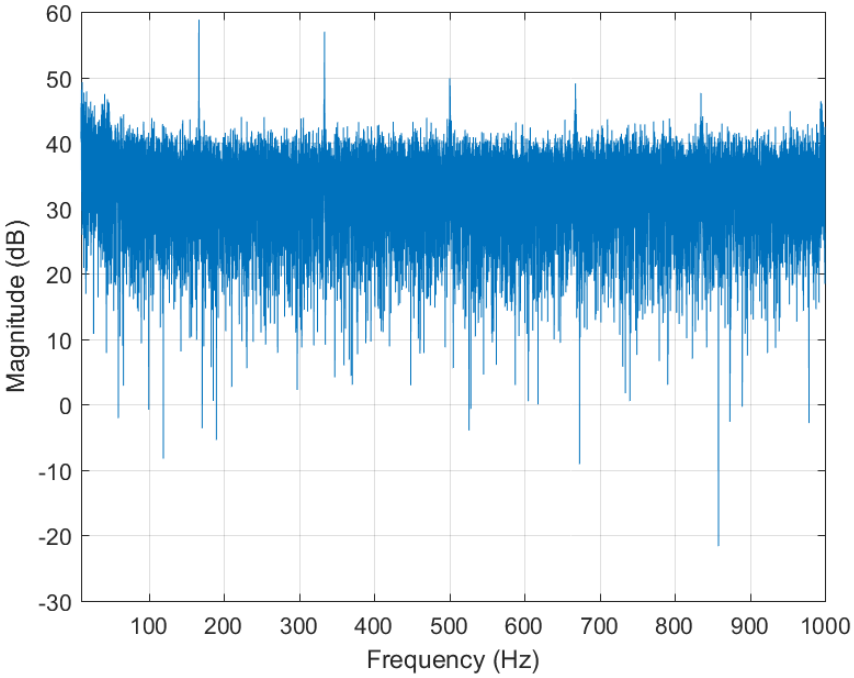

Figure A.11: Power optimized rotor noise, location 11

Table A.1: Difference in magnitude of peaks generated by the two blade types across various matching frequencies and locations

Location	Approximate Frequency (Hz)	Gain (Reduced Vortex – Power Optimized, dB)
5	334	1.11
5	668	1.09
5	835	-1.74
6	167	5.40
6	334	0.143
6	501	1.55
6	668	2.07
6	835	2.84
6	996	1.34
7	167	0.502
7	334	-0.728
7	501	-3.36
7	668	-1.18
7	835	2.23
8	167	-2.60
8	334	8.07
8	501	3.76
8	668	3.50
9	167	-5.15
9	334	2.38
9	501	0.822
9	668	2.11
10	167	-0.838
10	334	3.59
10	501	0.592
10	668	-2.39
10	835	0.573
11	167	6.39
11	334	0.490
11	501	0.400
11	668	1.55
11	835	0.371